PHYSICS OF PLASMAS **25**, 062508 (2018)

Comprehensive 3-D simulation and performance of ITER plasma facing and nearby components during transient events—Serious design issues

V. Sizyuk[a] and A. Hassanein[a]

Center for Materials Under Extreme Environment (CMUXE), School of Nuclear Engineering Purdue University, West Lafayette, Indiana 47907, USA

(Received 21 February 2018; accepted 2 June 2018; published online 25 June 2018)

A key obstacle to a successful magnetic fusion energy production in Tokamak reactors is performance during abnormal events. Abnormal events include plasma disruptions, edge-localized modes (ELMs), vertical displacement events, and runaway electrons. While tremendous efforts are being made to find ways to mitigate such events, a credible reactor design must be able to tolerate a few of these transient events. We have recently enhanced our comprehensive HEIGHTS (High Energy Interaction with General Heterogeneous Target Systems) simulation package to enable detailed 3-D investigation of the overall aspects of plasma-material interaction processes during all the transient events. Advanced models and numerical tools were developed to efficiently couple major key processes during the transient events, and in particular disruptions and giant ELMs. These include dynamic interaction, deposition, and scattering of the escaping core plasma particles with the evolving and propagating secondary divertor vapor/plasma in the strong magnetic field. These details are critical for assessing the damage to all interior components, including the hidden structure and the first wall which were not directly exposed to these transient events and never thought to be affected as a result. Despite developing numerous efficient numerical techniques and solution methods, such calculations take several months on current supercomputers to complete. Our present results show, for the first time, that unmitigated transient events could cause significant melting and vaporization damage to most interior and hidden components, including the first wall that were not directly exposed to these events. The current ITER divertor design may not work properly and need to be significantly modified or redesigned to prevent this damage. *Published by AIP Publishing.* https://doi.org/10.1063/1.5026597

I. INTRODUCTION

Successful development of future fusion reactors critically depends on the correct prediction of the heat and particle loads to the reactor walls and the optimum material choice for plasma facing components (PFCs). During the disruptive and transient operations in tokamak devices, the escaped core plasma particles are a potential threat to the lifetime of divertors and nearby components as well as the severe contamination issues from the eroded and splashed materials and from the developed secondary divertor plasma. Because of the high heat load and potential erosion of the surfaces in ITER and future DEMO operation, it is expected that the developed secondary plasma can severely affect the performance of PFCs and subsequent plasma operation following the transient events. Therefore, these issues should be studied very carefully in current existing small tokamak devices and comprehensively simulated in full reactor geometry. Available experimental data of current tokamak devices and theoretical predictions show that future ITER-like surfaces should be resistant both to a steady state heat flux of up to 20 MW/m^2 and to major transient ($\tau = 0.1$–10 ms) events of up to 10 GW/m^2. These values are estimates based on the current understanding and extrapolations from existing devices. High particle and heat fluxes can cause high surface sputtering erosion, melt and vaporization erosion, plasma contamination, and possible component failure that can disrupt the expected normal and safe operation of the reactor. The reactor geometry, the magnetic configuration, and the interaction processes in the scrape-off layer (SOL) determine not only heat transport and loads to component surfaces, but also play an important role in plasma confinement and control the transition to the H-mode operation. The interaction of the developed secondary plasma with component surfaces affects the behavior of D/T bulk plasma and impurity contaminations, influences toroidal plasma motion, and redistributes energy loads among interior reactor components.

Longstanding investigations of plasma confinement in fusion devices show that energy and particle transport across the magnetic field is determined with complex self-consistent turbulent physical processes in the core plasma.[1] Although the plasma instabilities responsible for the anomalous losses are known, the theory of these nonlinear processes is not developed enough to predict core plasma lifetime; only based on first principles. Therefore, various scaling rules based on the parameters of existing tokamaks are used to estimate and predict future reactor performance.[2] Statistically estimated methods based on current tokamaks predict that the core plasma lifetime increases with the core size R, plasma current I_p, and elongation $k = b/a$ and decreases with heating power P as

$$\tau \sim \frac{R^2 k^{0.9} I_p^{0.9}}{P^{0.66}}. \qquad (1)$$

---

[a] Electronic addresses: vsizyuk@purdue.edu and hassanein@purdue.edu

This scaling shows that, for ITER size devices $R = 6$–7 m and plasma current $I_p \sim 20$ MA, the plasma lifetime τ is more than 5 s for the power $P \sim 1$–1.5 GW. In addition to the scaling laws, special prediction rules are formulated for future large size tokamaks.[3] These include magnetic configuration, H-mode parameters, core plasma concentration and pressure, divertor, and the quasi-stationary operation with control of the main instabilities. Taking into account the scaling and selection rules, the average parameters of ITER tokamak transient events of the edge localized modes (ELMs) and disruptions were estimated.[3–5] Predictions of these transient event parameters vary in the literature. For example, the most common approaches[4] predict for ITER design that the pedestal energy $W_{ped} = 105$ MJ and plasma temperature of pedestal $T_{ped} = 3.3$ keV with frequency $1 - 100$ Hz. The event duration can be estimated based on the time of energy transport from the pedestal to the divertor target along the open field lines $\tau_{||} = 2\pi R q_{95}$. For ITER, this value is ~ 0.24 ms. To determine the final divertor fluxes, the corresponding wetted area on the divertor plate during these events should be estimated. For consistency with ITER design parameters, the corresponding wetted area during ELMs (for a modest broadening of ~ 1.5) is ~ 4.6 m^2 for the reference design and ~ 7.6 m^2 for a more inclined target.[6] The published data predict that the full pedestal energy will be released during disruptions and approximately $\sim 10\%$ of this energy can be released during giant ELMs. These simple calculations using these values predict the power density on the divertor surface flux to be ~ 10 MW/cm^2 for a disruption and ~ 1 MW/cm^2 for an ELM correspondingly. Implementing these numbers in computer simulations, the divertor surface erosion and component life-time can be evaluated.[4,5,7] Simulation assuming a localized divertor surface without taking into account the hydrodynamic evolution through the scrape-off layer (SOL) can only crudely predict the response of the divertor plate. The unstable and oscillating character of tokamak operations adds additional uncertainties into the estimated average values.[8] Even the low ELM particle flux is expected to cause the tungsten divertor to melt, vaporize, and form secondary plasma. While the radiation and the particle flux of this ELM generated secondary plasma may not be high to cause further damage, the expansion and propagation of this secondary plasma through the SOL and potentially penetrating into the core plasma could cause serious contamination and possible plasma termination through disruption. This problem is complicated to solve and requires integrated models where the secondary plasma dynamic plays the leading role.[9] In this work, we present new enhanced integrated models that accurately describe the plasma facing component response to a wide range of ELMs and disruption parameters in real 3D ITER-like geometry and operating conditions.

The incident escaping core plasma is usually unsteady in space and time and will interact with the developed and evolving secondary divertor plasma initiated during the very early impact of the disrupting main core plasma. Over the years, we have developed multidimensional models for extensive and integrated simulation of the escaped core plasma deposition and interaction with the divertor and nearby components.[10] The disrupting escaped core plasma initiates particle evolution (i.e., motion and scatterings) in full realistic 3D ITER geometry in the presence of both magnetic and electric fields starting from the last closed flux surface (LCFS) through the entire SOL area and up to the penetration depths inside the divertor components. We have implemented, verified, and benchmarked numerical methods in our High Energy Interaction with General Heterogeneous Target Systems (HEIGHTS) simulation package including our new 3-D Monte Carlo (MC) kinetic model to study the spatial profile of ion and electron energy depositions of the escaped core particles in both inner and outer divertor plates for both NSTX and ITER device parameters. This includes a detailed magnetic field complex structure and actual geometry of various components. Our previous calculations showed good agreement of the energy deposition profiles with various experimental data without using any additional fitting parameters.[10] The initial simulation conditions included three main parameters: (1) pedestal energy $W_{ped} = 126$ MJ, (2) temperature of pedestal $T_{ped} = 3.5$ keV, and (3) event duration $\tau = 0.1$–3.0 ms to cover all possible transient duration ranges. Based on these parameters, we used a total of 126 MJ for the disruption and 12.6 MJ for giant ELMs. Figure 1 shows the typical energy deposition profile predicted along the divertor plate surface in the poloidal direction at the initial time t = 0.0 ms of a disruption event with 3.0 ms duration.[10]

The power loading asymmetry between the inner and outer divertor sides is well known and actively studied in recent years as a result of the core particle drift and separation phenomena.[11,12] The heat load profile and the resulting divertor surface erosion have a non-ideal exponential profile beginning at the strike point due to the shift and separation of the escaped core plasma ions and electrons. Significant contribution to this process is caused by the magnetic field drifts, ballooning transport on the low field side, and various geometrical effects.[13,14] Many experimental studies in

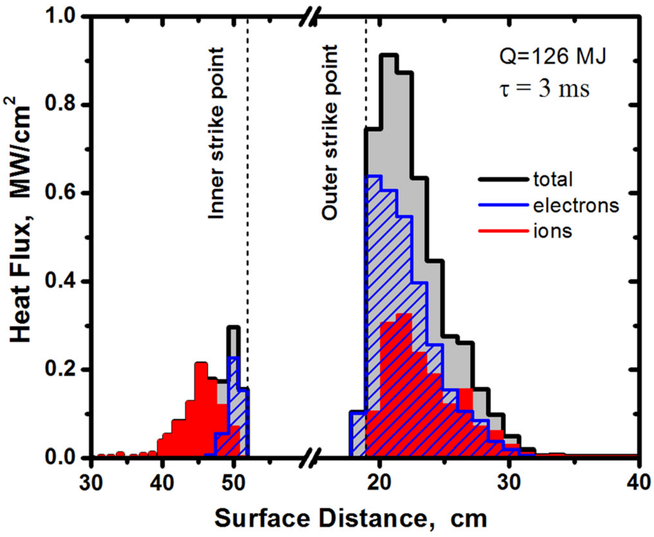

FIG. 1. HEIGHTS Monte Carlo simulation of initial power flux on the ITER divertor plate surfaces for 3.0 ms disruption: inner divertor plate (left) and outer divertor plate (right). The surface distance axis is assumed along the perimeter of the tokamak poloidal cross-section.

tokamaks have shown the distorted character of the heat load distributions and surface damage during the loss of stability events.[15–17] This was explained by the magnetic drift and induced magnetic perturbations in the presence of the impurity transport.[18] We enhanced and build on these models taking into account the various scattering processes of the escaped core particles during the evolution of secondary divertor plasma. The details of radiation transport (RT) in the evolving secondary plasma were extensively developed and implemented into the integrated models. The calculations initially started from the equilibrium magnetic field configuration extracted from the EQDSK database files.[19,20] Contrary to using an average value, the predicted energy deposition profile corresponds to an exponential distribution with the maximum $\sim 0.9\,\mathrm{MW/cm^2}$ located near the strike point. We predicted the maximum power flux values for the expected full range of possible ELMs and disruptions in the ITER device.

The 3-D kinetic Monte Carlo model of the escaping core plasma particles was developed for self-consistent analysis of the magnetohydrodynamic (MHD) evolution of the developed secondary divertor "mini" plasma where the escaping particles are used as the input volumetric power source. Our previous study of this secondary plasma showed significant conversion of the incident disrupting plasma particle energy to photon radiation to several nearby components.[5,10] Contrary to the main core plasma, the secondary divertor plasma is much denser, colder, heavier, and not fully ionized. The MHD of the generated secondary plasma dominates the divertor space, i.e., the impact of the D/T plasma during the loss of core confinement can be considered as a small perturbation and an energy source feeding this evolving plasma.

A simple estimation from the energy deposited onto the divertor surface during core plasma instabilities predicts a massive flow of the divertor material with density up to $\sim 10^{17}\,\mathrm{cm^{-3}}$ near the original surface that is much higher than the SOL D/T plasma values $\sim 10^{13}\,\mathrm{cm^{-3}}$. The secondary plasma characteristics and conditions allowed the implementation of recent comprehensive models developed and extensively benchmarked in our HEIGHTS for laboratory plasma devices. The MHD, atomic physics, radiation transport, and heat conduction processes can be simulated in the dense evolving secondary plasma similarly to laser- or discharge-produced plasma devices currently proposed for advanced nanolithography.[21] As noted above, behavior of the secondary plasma was well studied around the local divertor areas where a specific design of divertor components was not fully taken into account. At the same time, we showed that the radiation fluxes generated in secondary plasma are comparable in magnitude to the direct core plasma impact.[5,10] Using the developed gyrokinetic model of the escaping core plasma, we simulated the full evolution of the secondary plasma starting from the initiation and drift along tokamak components, and the expansion through the entire SOL. The integrated model included heating and erosion of component surfaces, vaporization, ionization, and secondary plasma formation, secondary plasma MHD, heat conduction, and photon radiation transport. We note again that the MHD equations are applied here not to the hot D/T rarefied disrupting core plasma but related to the MHD of secondary plasma of the divertor plate and the MC kinetic flow of the escaped core particles is the energy source feeding this plasma. The density of this secondary plasma is much higher than the disrupting core plasma and is not fully ionized compared to the core plasma. The input energy of the escaping core plasma to the MHD equations is simulated by our kinetic MC model.

It should be noted that the drift of the escaped core particles due to the gradient of the magnetic field has an opposite flow direction for ions and electrons. The large mass difference between these particles and the resulting differences in Larmor radii makes the escaping probability of core plasma different for electrons and for ions. The radial electric field appears due to charged particle separation around the LCFS. Therefore, this results in specific spatial shaping and shifting of the energy deposition profile along the divertor surface as shown in Fig. 1. The details of the equations of motion of charged particles in the arbitrary directed magnetic and electric fields implemented in HEIGHTS are not shown here; however, the spatial and temporal parameters of the escaped core plasma flow in the magnetic and electric fields in the SOL are described in detail in Ref. 10.

The goal of this work is to simulate the secondary plasma evolution, propagation, and interactions with various reactor components following disruptions and ELMs originally incident on both divertor plates, i.e., inner and outer plates. As previously shown in our simulation, the component damage is mainly determined from the secondary dense divertor plasma evolution and propagation than from the initial rare core plasma impact. The maximum energy delivered to the divertor plate during the transient events of the current ITER design is assumed to be 126 MJ for hard disruptions and 12.6 MJ (10% of the total) during giant ELMs. The maximum power flux on the divertor plate during these events will depend on the transient event duration. The transient event duration was varied from $\tau = 0.1$–$3.0\,\mathrm{ms}$ to cover a wide range of uncertainties as discussed before. We have implemented in HEIGHTS the exact original ITER full 3-D geometry with all fine design details to predict the response of all exposed and interior surfaces including inner and outer divertor plates, inner and outer reflector plates, inner and outer baffles, inner and outer stainless steel "umbrella" tubes, dome structure, and the lower parts of the inner and outer Be first walls. In this analysis, we considered all sources of energy deposition to these components including the original escaping plasma particles, radiation of the secondary plasma from the divertor material, and the deposition of the escaped core particles due to various scattering processes from the dense evolving and propagating secondary plasma plume.

II. MODEL DETAILS

HEIGHTS integrated models are continuously being enhanced to include fine details of various reactor geometries (e.g., ITER, NSTX, etc.) for the full 3-D simulation of the reactor environment (e.g., Fig. 2). We developed, for the first time, a comprehensive kinetic Monte Carlo model for the simulation of the escaping core plasma and for the prediction of heat load to all plasma-facing components using the entire 3D device geometry. The detailed description of the escaping core particles into the SOL was implemented into the integrated model to be used as the input volumetric power source in the MHD module.[10] Based on the various advantages of the splitting processes used in solution of the transport problem, our upgraded model includes both of the two separated subtasks (i.e., MC and MHD); however, we do not use any fitting parameters or averages from continuum media, i.e., we do not solve Navier-Stokes equations for the escaped core D/T plasma. All the physical processes included into HEIGHTS integrated modules are interconnected. For example, the escaped core plasma particles initiate divertor surface vaporization and further vapor heating leading to the secondary plasma formation. Further energy deposition and heating by the incident disrupting core plasma particles define the dynamics of the secondary plasma evolution and its propagation along nearby components. The MHD evolution of the secondary plasma redistributes the density temporal and spatial profiles in SOL and consequently changes the scattering processes and the interactions of the escaping core particles. We simulate the motion of the escaping core plasma as individual particles composed of deuterons, tritons, and electrons escaping along the complex electromagnetic field structure of the entire device. The advantages of our approach are the ability to study various drift phenomena, to separately divide the contribution of different ions and electrons into component heat loads, and to exclude artificial fitting parameters usually used in the description of anomalous transport properties. The particle motion is calculated using ab-initio models with simulation of all possible scattering processes and their probabilities along their path.

The quadtree adaptive mesh refinement (AMR) algorithms with 5-level sublayers were developed and implemented in HEIGHTS to significantly enhance the accuracy of the calculation and to reduce the extensive required computational time. We use these hierarchy levels for the accurate initialization of the complex geometry of the tokamak component surfaces for the entire divertor and SOL areas starting from the submicron level size, up to millimeter size MHD cells located near surfaces, and meter size reactor component systems. For the undersurface processes, additional refinement is used with cell sizes ~0.5 μm.

Analogous to our previous studies,[10] we constructed the integrated models and packages in such a coordinate system where the secondary plasma MHD equation set is used as the model core

$$
\begin{aligned}
&\frac{\partial\rho}{\partial t}+\frac{1}{r}\frac{\partial}{\partial r}(r\rho v_r)+\frac{\partial}{\partial z}(\rho v_z)=Q_m^{vap},\\
&\frac{\partial\rho v_r}{\partial t}+\frac{1}{r}\frac{\partial}{\partial r}\left[r\left(\rho v_r^2-\frac{B_r^2}{4\pi}\right)\right]+\frac{\partial p_t}{\partial r}+\frac{\partial}{\partial z}\left(\rho v_r v_z-\frac{B_rB_z}{4\pi}\right)=\frac{\rho v_\varphi^2}{r}-\frac{B_\varphi^2}{4\pi r},\\
&\frac{\partial\rho v_\varphi}{\partial t}+\frac{1}{r}\frac{\partial}{\partial r}\left[r\left(\rho v_\varphi v_r-\frac{B_\varphi B_r}{4\pi}\right)\right]+\frac{\partial}{\partial z}\left(\rho v_\varphi v_z-\frac{B_\varphi B_z}{4\pi}\right)=\frac{\rho v_\varphi v_r}{r}-\frac{B_\varphi B_r}{4\pi r},\\
&\frac{\partial\rho v_z}{\partial t}+\frac{1}{r}\frac{\partial}{\partial r}\left[r\left(\rho v_z v_r-\frac{B_zB_r}{4\pi}\right)\right]+\frac{\partial}{\partial z}\left(\rho v_z^2+p_t-\frac{B_z^2}{4\pi}\right)=0,\\
&\frac{\partial e_h}{\partial t}+\frac{1}{r}\frac{\partial}{\partial r}\{r[v_r(e_h+p_h)]\}+\frac{\partial}{\partial z}[v_z(e_h+p_h)]=Q_{en}^{vap}+Q_{hc}+Q_J+Q_{imp}+Q_{rad},\\
&\frac{\partial B_r}{\partial t}+\frac{\partial}{\partial z}(v_zB_r-B_zv_r)=Q_r^{md},\\
&\frac{\partial B_\varphi}{\partial t}+\frac{\partial}{\partial r}(v_rB_\varphi-B_rv_\varphi)+\frac{\partial}{\partial z}(v_zB_\varphi-B_zv_\varphi)=Q_\varphi^{md},\\
&\frac{\partial B_z}{\partial t}+\frac{1}{r}\frac{\partial}{\partial r}[r(v_rB_z-B_rv_z)]=Q_z^{md}.
\end{aligned}
\tag{2}
$$

Equations (2) express the conservation laws for mass, momentum, energy, and magnetic field given in the cylindrical coordinate system (Fig. 2) where the φ - components were integrated. Here, ρ is plasma density; v is plasma velocity; B is magnetic field; $p_t=p_h+p_m$ is total pressure including hydrodynamics and magnetic parts; $e_h=e_i+e_k$ is total hydrodynamic energy including internal and kinetic energy of plasma. The equation system describes the convective motion of the secondary plasma and should be coupled with the dissipative physical processes such as the heat conduction, radiation transport, magnetic diffusion, and the core plasma energy deposition during the transient events. We took into account these processes as the right-side sources in Eqs. (2), which should be dynamically recalculated in parallel to the main MHD solution. The source terms in the right side include: Q_{hc} is thermal conduction source, which determines the solution of the heat conduction equation; Q_{rad} is the radiation source, which determines the solution of the RT block; Q_J is the Joule heat term, which determines the effect of Joule heating currents induced in plasma; ${Q_m}^{vap}$ and

${Q_{en}}^{vap}$ are target vaporization mass and energy; Q_{imp} is the core plasma source, which determines the energy deposited by escaped core particles, also determines the solution of the MC particle impact term; and Q^{md} is the magnetic diffusion term, which determines the solution of the resistive part of the magnetic field equations. Generally, the source terms are the solution results of the additional equations that describe the specific physical processes of the various sub-problems. The source terms adjust the transport model by taking into account the anisotropic transport properties that incorporate radial and toroidal solutions into Eqs. (2). The detailed description of the source term application is shown in detail in Refs. 5, 9, 10, and 22.

To reduce the extensive mathematical description and using the total variation diminishing (TVD) numerical method in the Lax-Friedrichs (LF) formulation,[23] we can express Eqs. (2) in the following matrix form:

$$\frac{\partial \mathbf{U}}{\partial t} + \frac{1}{r}\frac{\partial}{\partial r}[r\mathbf{F}(\mathbf{U})] + \frac{\partial \mathbf{P}(\mathbf{U})}{\partial r} + \frac{\partial \mathbf{G}(\mathbf{U})}{\partial z} = \mathbf{\Omega}, \qquad (3)$$

where

$$\mathbf{U} = \begin{bmatrix} \rho \\ \rho v_r \\ \rho v_\varphi \\ \rho v_z \\ e_h \\ B_r \\ B_\varphi \\ B_z \end{bmatrix}, \quad \mathbf{F}(\mathbf{U}) = \begin{bmatrix} \rho v_r \\ \rho v_r^2 - B_r^2/4\pi \\ \rho v_\varphi v_r - B_\varphi B_r/4\pi \\ \rho\, v_z v_r - B_z B_r/4\pi \\ v_r(e_h + p_h) \\ 0 \\ 0 \\ v_r B_z - B_r v_z \end{bmatrix},$$

$$\mathbf{P}(\mathbf{U}) = \begin{bmatrix} 0 \\ p_t \\ 0 \\ 0 \\ 0 \\ 0 \\ v_r B_\varphi - B_r v_\varphi \\ 0 \end{bmatrix}, \quad \mathbf{G}(\mathbf{U}) = \begin{bmatrix} \rho v_z \\ \rho v_r v_z - B_r B_z/4\pi \\ \rho v_\varphi v_z - B_\varphi B_z/4\pi \\ \rho v_z^2 + p_t - B_z^2/4\pi \\ v_z(e_h + p_h) \\ v_z B_r - B_z v_r \\ v_z B_\varphi - B_z v_\varphi \\ 0 \end{bmatrix} \qquad (4)$$

and all right terms are combined in source matrix $\mathbf{\Omega}$

$$\mathbf{\Omega} = \begin{bmatrix} Q_m^{vap} \\ \rho v_\varphi^2/r - B_\varphi^2/4\pi r \\ \rho v_r v_\varphi/r - B_r B_\varphi/4\pi r \\ 0 \\ Q_{en}^{vap} + Q_{hc} + Q_J + Q_{imp} + Q_{rad} \\ Q_r^{md} \\ Q_\varphi^{md} \\ Q_z^{md} \end{bmatrix}. \qquad (5)$$

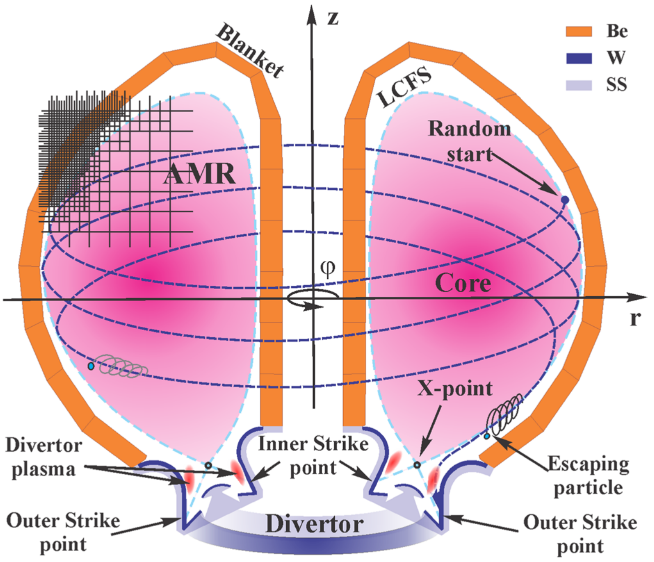

FIG. 2. Schematic of ITER components and orientation of the coordinate system used in our HEIGHTS simulations.

The matrix form of Eq. (3) expresses in short form the formation and the drift of the secondary plasma of the divertor plate material with the parameter ρ is the density of the secondary plasma (tungsten in this case) and not the core fuel D/T plasma density. The clean D/T plasma particles escaping the core during the transient events will initially come into collision with the divertor component surfaces and deposit their energy initiating the formation of this secondary plasma. Because the density of core plasma ($\sim 10^{13}$ cm^{-3}) is very small in comparison to the secondary plasma ($\sim 10^{17}$ cm^{-3}), it is reasonable to construct and use the gyrokinetic model to simulate the core plasma impact and to use the MHD model for the secondary plasma evolution. These conditions allow treating the secondary plasma evolution as the main driving source and the core/SOL plasma processes as a dynamic external input source to this main evolving and propagating divertor plasma throughout the divertor area and SOL regions.[10] The large difference in densities between the core and the secondary plasmas allowed us to take into account only the energy term in Eq. (2) and to avoid for example the mass term. Our preliminary simulations for ITER geometry showed that the escaped core particle can make ∼5–6 rotations along the tokamak toroidal geometry before arriving at and penetrating into component surfaces. Assuming that the initial escaping plasma temperature is 3.5 keV, the escaped core plasma particles can arrive in time comparable with the shortest transient event duration, i.e., ∼0.1 ms. Because the main goal of this study is assessing the potential damage of ITER device components, we assumed that the start time point of the transient event simulation is the arrival of the particles at the divertor plate surface. A direct full MC simulation where the full ensemble of escaping core particles should be simulated during the transient event time is not realistically feasible due to limitations in current computer power and memory. The full particle data should be stored in memory for the time of the MHD and other operation steps. To decrease the calculations volume, various simplifications can be applied, e.g., transformation of the SOL to a lower dimensional option.[24]

In our recently developed models in the enhanced HEIGHTS package, we however, calculate various particles flow every MHD time step starting from the LCFS and finishing at components surfaces. The integration of these particular solutions for each time step provides the solution of the general dynamic problem similar to our previously developed solutions for the heat conduction and magnetic diffusion problems.[22] For simulating a transient event, we assumed instantaneous continuous particle flow, which appears from the time moment $t_0 = 0$ and ends at the event finish time. The intensity of the particle flow is assumed equal to the current transient event intensity based on energy conservation laws.

To preserve the multiscale approach in our integrated physical and mathematical models and to ensure reasonable accuracy, we used the adaptive mesh refinement (AMR) algorithms with unstructured grid geometry[25] and applied the TVD-LF method to the quadtree mesh in the finite volume approach. The details of such implementation can be found in Ref. 7. As shown in Eq. (5), the secondary plasma initiation is controlled by the terms $Q_m{}^{vap}$ and $Q_{en}{}^{vap}$, where the $Q_m{}^{vap}$- term describes the mass of the vaporized material (W) moved from the solid wall into the hydrodynamic computational domain and the $Q_{en}{}^{vap}$-term describes correspondingly the energy of this vapor moved to the domain. Calculation of these terms is based on the energy deposition into the solid walls following the MC model of the escaping core plasma.[10] The gyrokinetic model determines evolution of the fuel plasma particles (D, T, and e) starting from escaping the LCFS, motion through the SOL including both toroidal rotation and Larmor gyration, and ending in the solid/liquid matter of the tokamak components. The particle evolution included also various possible events: (1) return back into the core plasma, (2) scattering in the SOL from the secondary evolving divertor plasma or from the neutral vapor of the divertor cold vaporized material, (3) penetration into the liquid/solid matter of the component as well as scattering underneath the surface, and (4) collisional cascade processes and slowing down inside the target materials. Penetration into the solid matter and scatterings processes under the surface determine the spatial energy deposition in the walls due to the core plasma impact and the resulting appropriate thermal response. Subsequent solution of the heat conduction problems in the solid/liquid material provides the resulting vapor amount needed to initiate the MHD evolution of the divertor material. Here, we stress that the MC recalculations should be done dynamically, i.e., in parallel to the MHD processes to have accurate energy deposition into the secondary plasma, vapor, and solid wall.[10]

The newly developed MC model of core plasma particle evolution includes eight main scattering processes: ion-nuclear interactions, ion-electron interaction, electron-nuclear interaction, electron-electron interaction, Bremsstrahlung process, Compton processes, photoabsorption, and Auger recombination. A brief description of these processes is given below. The developed MC model is based on approximation of binary or pair collisions.[26] This approximation allows us to assume particle trajectory as a zigzag line of combined sections between separate nuclear interactions and electronic losses. Depending on the target material, the frequency of scattering varies and can be up to $\sim 10^5$ individual interactions for the slowing down of ions and electrons in metal the energy ranges encountered in Tokamak plasmas. Because one cannot take into account all these separate interactions, all collisions are separated on two groups: close collisions and distant collisions. The probability for close or distant collision is determined mainly from the incident particle mass, energy, and the target material. The distant interaction results (for example, electronic friction losses) are accumulating on the trajectory and are added along the moving particle pathway.

The ion-nuclear scatterings were calculated in the Thomas-Fermi potential approach[27]

$$\sigma_{in} = \frac{C_k}{k\,E^k}\frac{T_{\max}^k - T^{*k}}{T_{\max}^k\,T^{*k}}, \tag{6}$$

where the cross-section of ion nuclear scattering σ_{in} is a function of the initial ion energy E and transferred energy T. Here, $T_{\max} = \frac{4m_i m_n}{(m_i+m_n)^2}E$ is the maximum possible energy transferred due to scattering from an ion with mass m_i to the nucleus with mass m_n. We assumed 5% boundary between the close and distant collisions: $T^* = T_{\min} + 0.05\,(T_{\max} - T_{\min})$, where the minimum transferred energy T_{min} for solid can be taken as the defect formation energy T_d or for gas calculated from minimum deviation angle $\theta_{\min} = h/(m_i v_i a_{TF})$. In this expression, h is Plank constant, v_i is the ion velocity, and the Thomas-Fermi distance is given

$$a_{TF} = \frac{1}{2}\left(\frac{3\pi}{4}\right)^{2/3} a_B\left(z_i^{2/3} + z_n^{2/3}\right)^{-1/2}, \tag{7}$$

where z is particle charge and $a_B = \hbar^2/(m_e e^2)$ is the Bohr radius. The coefficient C_k was determined for three energy ranges of the ion, i.e., for $k = 1$, 1/2, or 1/3

$$C_k = \frac{1}{2}\pi\lambda_k a_{TF}^2\left(\frac{m_i}{m_n}\right)^k\left(\frac{2z_i z_n e^2}{a_{TF}}\right)^{2k}, \tag{8}$$

with

$$\begin{cases} k = 1, & E > 1\,\text{MeV}, & \lambda_1 = 0.5 \\ k = 1/2, & 50\,\text{keV} < E \le 1\,\text{MeV}, & \lambda_{1/2} = 0.327 \\ k = 1/3, & E \le 50\,\text{keV}, & \lambda_{1/3} = 1.309. \end{cases}$$

The Born approximation[26] was used for modeling ion-electron interactions σ_{ie}

$$\frac{d\sigma_{ie}}{dT} = \frac{2\pi z_{eff}^2 m_e r_e^2 c^4}{v_i^2}\left(1 - \frac{v_i^2}{c^2}\frac{T}{T_{\max}}\right)\frac{1}{T^2}, \tag{9}$$

where $r_e = e^2/(m_e c^2)$ is the electron classical radius and c is the speed of light. The ion effective charges z_{eff} can be found in Refs. 28 and 29. The main purpose of our study is accurate energy deposition and redistribution during the core particle interaction with the secondary plasma, vapor, and wall components. As we are modeling the energy transfer into the target, we focus our attention in this modeling on the most probable and "energy transferable" collisional processes. For example, it is not important to discuss here about the close ion-electron collisions due to very small energy transfer between two particles with a very large mass difference. We took into account the averaged energy transfer in distant collisions and used the Linhard and Bethe models to calculate the energy losses.[26,28] Linhard stopping power describes well the low energy ion scatterings and Bethe theory is developed for higher energy of the incident ions.[26] We combined both theories using a special fitting factor as described in our Ref. 30. The revised methods consider these collisions with the Larmor trajectories and on the quadtree mesh.

In tokamak conditions, the most probable energy of the escaped core electrons is usually lower than 100 keV with the clear majority of particles having no more than 10 keV. In this case, the electron-nuclear collisions can be sufficiently described using Rutherford theory in the Mott representation for electrons[31]

$$\frac{d\sigma_{en}}{d\Omega} = \left(\frac{z_n e^2}{4E}\right)^2 \frac{1}{\sin^4(\theta/2)}, \qquad (10)$$

where z_n is the charge of nucleus, θ is the scattering angle, and e is the electronic charge. Introducing the interfacial scattering angle θ^* to separate the close and distant collisions (see the above similar procedure for transferred energy T), we can integrate Eq. (10) over the possible angles $\theta \in [\theta^*; \pi]$ to calculate the full cross-section of the electron-nuclear interaction

$$\sigma_{en} = \pi\left(\frac{z_n e^2}{2E}\right)^2 \frac{1+\cos\theta^*}{1-\cos\theta^*}, \qquad (11)$$

where the kinematic relation for the transferred energy is given

$$T = 4\frac{m_e m_n}{(m_e+m_n)^2} E\sin^2(\theta/2), \qquad (12)$$

and the scattering angle for the inlet electron can be sampled following the Neumann method[32]

$$\cos\theta = \frac{2(1-\cos\theta^*)}{\xi(1+\cos\theta^*)-2} + 1, \qquad (13)$$

where $\xi \in [0; 1]$ is a random number. In this study, particular interest is when the energetic particle can significantly change the initial direction [Eq. (13)] or the target particle can gain significant energy and also change the initial moving direction as in the electron—electron close collisions. Such scattering processes can induce particle jumps where particles can change the magnetic field line as schematically shown in Fig. 3 (right side). The left side of Fig. 3 illustrates the structure of the initial magnetic field lines of the ITER device as taken from the EQDSK files.[11,12] The scatterings change the local Larmor gyration center in the poloidal plane, i.e., change of the **B**—line that defines the toroidal motion of particle in the entire SOL area. Contrary to the models where particle motion is directly associated with the gyration center without the spiral motion analysis (so called guiding center approximation),[33–35] we simulated close particle collisions on the real spiral trajectories to trace the final incident points of the escaped core particles as well as the scattered particles from the evolving plasma on component surfaces. This detailed dynamic interaction of the escaping core plasma particles with the evolving and expanding secondary plasma cloud can result in intense pulsed energy loads in unexpected spots on component surfaces. This could result in additional damage to these areas that otherwise only see radiation flux from the expanding plasma cloud.

The electron-electron scattering implemented in our models follows Møller theory.[36] The full cross-section of the close collisions was calculated by integrating the Møller differential cross-section for the energy interval $T \in [T^*; T_{max}]$ and is given by

$$\sigma_{ee} = \frac{\pi e^4}{E}\left[\frac{E-2T^*}{T^*E} + \frac{E-2T^*}{E(E-T^*)} + \frac{1}{E}\ln\left(\frac{T^*}{E-T^*}\right)\right]. \qquad (14)$$

The acceptance-rejection method[37] gives the following kinematic relation for the energy transferred

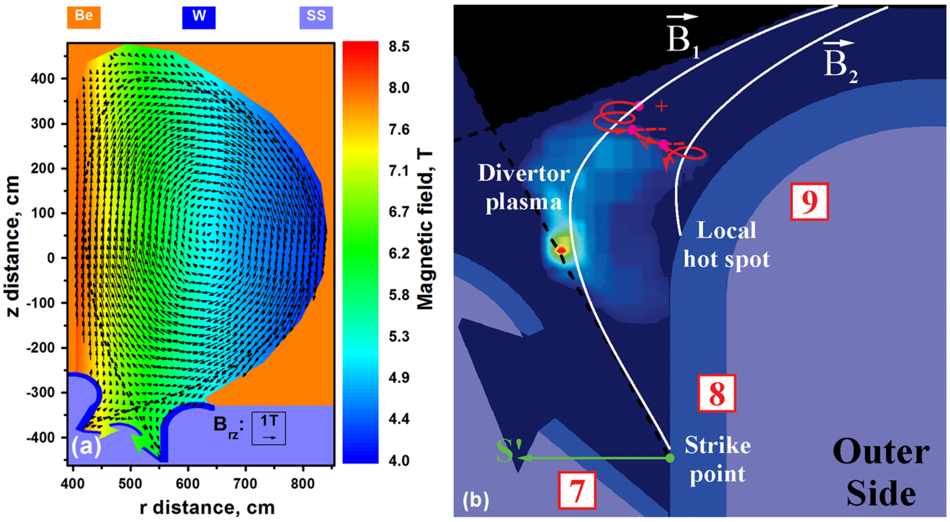

FIG. 3. Illustration of the ITER initial magnetic field structure (a) and particle jump from the B_1 to the B_2 magnetic field lines due to collisions (b).

$$T = \frac{T^*E}{E - \xi_1(E - 2T^*)}, \quad \xi_2 < 1 - \frac{T(E - 2T)}{(E - T)^2}. \tag{15}$$

Here, ξ_1 and ξ_2 are random numbers. The scattering angle is calculated from sampled energies as $\cos\theta = \sqrt{1 - T/E}$.

The collisions with the photon process were calculated according to the model developed for the runaway electron study.[38] The photoabsorption cross-section depends essentially on the charge of the medium nuclei and the photon energy. For our case of low energies (<0.2 MeV), the absorption cross-section is proportional to $1/E_{ph}^3$. The differential cross-section of photoabsorption is then written in the following form:[26]

$$\frac{d\sigma_{ph}}{d\Omega} = \sigma_n(E_{ph}) \sin^2\theta \cos\varphi \, (1 + 4\beta\cos\theta), \tag{16}$$

where $d\Omega$ is the solid angle of the ejected photoelectron; $\sigma_n(E_{ph})$ is the cross section of photoabsorption at the corresponding shell; θ and φ are the polar and azimuthal angles; $\beta = v/c$; and v is the photoelectron velocity. The σ_n is determined from the result of quantum mechanical calculations in accordance with the Hartree-Fock-Slater model.[39] We also assumed that the Auger photons generated by relaxation of electron shells are absorbed within the same calculation cell due to their low energy.

In Compton scattering, a photon interacting with an atomic electron changes its direction and transfers part of its energy to the electron. This process dominates in the energy range up to 50 MeV for elements with low and medium atomic numbers.[40] We modeled the Compton scattering processes following the Klein-Nishina-Tamm model, where the differential cross section $d\sigma_{com}$ can be expressed as

$$\frac{d\sigma_{com}}{dE'_{ph}} = \frac{\pi r_e^2 m_e c^2}{E_{ph}^2}\left[\frac{E_{ph}}{E'_{ph}} + \frac{E'_{ph}}{E_{ph}} + \left(\frac{m_e c^2}{E'_{ph}} - \frac{m_e c^2}{E_{ph}}\right)^2 - 2m_e c^2\left(\frac{1}{E'_{ph}} - \frac{1}{E_{ph}}\right)\right], \tag{17}$$

which integrated to obtain the total scattering cross-section

$$\sigma_{com} = 2\pi r_e^2 \frac{N}{x}\left[\left(1 - \frac{4}{x} - \frac{8}{x^2}\right)\ln(1 + x) + \frac{1}{2} + \frac{8}{x} - \frac{1}{2(1 + x)^2}\right]. \tag{18}$$

Here, $x = \frac{2E_{ph}}{m_e c^2}$ is the reduced energy of the photon, and E'_{ph} is the scattered photon energy.

The radiation transport, heat conduction, and magnetic diffusion models did not undergo major changes from our previous description;[10,22,41] therefore, we restrict our model description using the references where these models were presented in detail. Our previous simulations[5] showed the potential high risk of component damage during transient events from the secondary plasma radiation. Following the above described models, the escaped core particles deposit part of their energy in the vapor and secondary plasma during the collisions. The vapor is then heated up, ionized, and forms a mini plasma with higher temperature with radiative cooling arising from this plasma with intense photon radiation out of this secondary plasma cloud that can cause surface damage in various interior and hidden locations. For detailed calculation of the secondary radiation, we developed a comprehensive Monte Carlo radiation transport (RT) model based on several weighted factors to significantly reduce the computational time. The implemented weight factors in our MC model greatly reduced RT calculations compared to both MC models without weight factors and the direct RT solution methods. The details of the MC RT methods executed for the quadtree mesh were published elsewhere.[10]

In calculating the radiation transport in plasma, the integral radiation fluxes depend to a great extent on the level of details and the precision of the plasma optical coefficients. In turn, the computational accuracy and the precision of the calculated opacities depend on the accuracy and the fine details of the atomic data. We have spent much effort in developing an extensive atomic data set for potential divertor materials including tungsten, carbon, and liquid metals. Because details of opacity and atomic data calculations are very extensive and beyond the objectives of this paper, we refer the readers to our previous publications.[42,43] Here, we note that the structure of atomic energy levels, wavefunctions, transition probabilities, ionization potentials, oscillator strengths, broadening constants, photoionization cross sections, and other atomic characteristics are calculated using our self-consistent model based on the Hartree-Fock-Slater (HFS) method.[39] The collisional radiative equilibrium (CRE) model[44] was used to calculate the populations of atomic levels and the ion and electron plasma populations. Because the CRE model satisfactorily describes the optically thin plasma, the escape probability approximation for line transitions and direct photoionization for the continuum spectrum was implemented to reduce nonlocal radiation effects.[45]

Figure 4(a) shows the schematic illustration of the radiation transport zone in the divertor Cassette and SOL areas. For each hydrodynamic cell in these areas, over 10^5 photons are used to simulate photon transport representing all possible photon energy in each cell. The photon spectra of each cell are generated depending on the temperature and density of that cell. Figure 4(b) shows sample detailed spectra for a certain cell temperature and density. Such calculations require significant computational time but are critical to the accuracy of such results and prediction of various damaged locations.

We integrated the above revised models of the MHD and core particles collisions with the RT transport models,[10] heat conduction models,[41] and magnetic diffusion models[22] to predict the dynamic behavior of the resistive and radiative evolving secondary divertor plasma subject to the evolution and bombardment of the escaping core plasma particles. The application of these integrated models to the ITER design including the entire Cassette and SOL areas allowed, for the first time, to predict the dynamic thermal response of plasma-facing and all nearby components including the first walls as a result of these transient events. The calculations predict unexpected serious potential damaged areas and hot spots at various component surfaces due to both the intense radiation of the evolving secondary plasma and from plasma

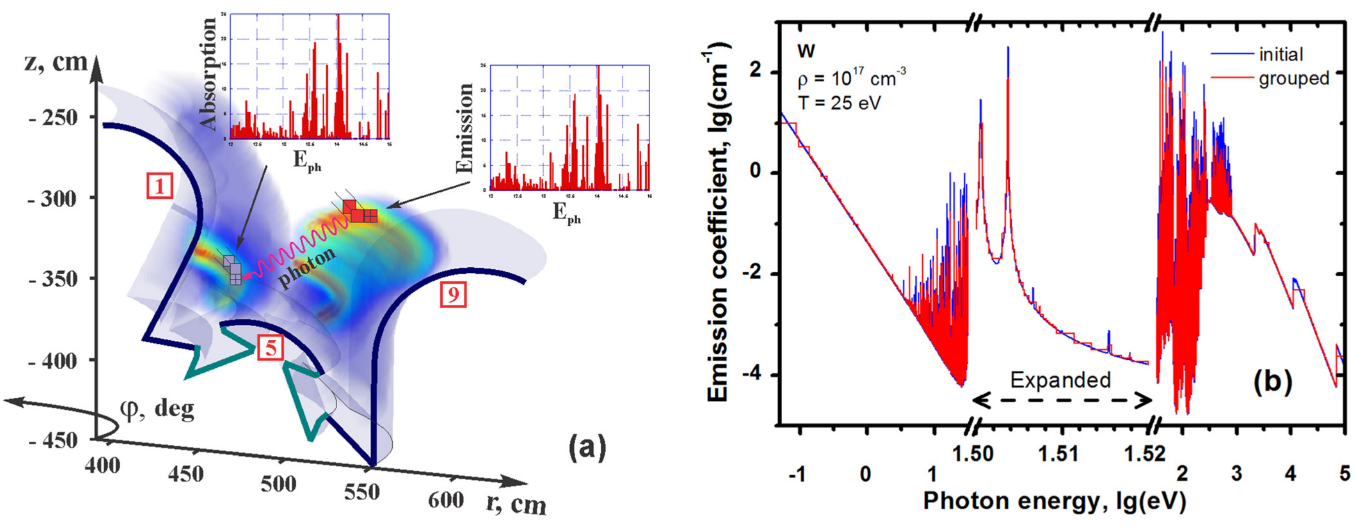

FIG. 4. Illustration of details of radiation transport calculation (a) and optical data refinement (b) of evolving plasma in the divertor Cassette area.

particle scattering and deposition on these components. Damage to hidden components and locations other than the original divertor plates can result in serious flaw in ITER operation and significant delays in repairing such hidden components.

III. SIMULATION RESULTS

The main goal of this work is, for the first time, to simulate the dynamic interaction of the escaped core plasma particle flow and the resulting secondary divertor plasma during transient disruptions and ELMs in full 3-D real ITER geometry with exact dimensions and to predict details of the thermal response and damage to various plasma-facing and surrounding components. These include inner and outer divertor plates, inner and outer reflector plates, inner and outer baffles, inner and outer stainless steel “umbrella” tubes, dome structure, and the lower parts of the inner and outer Be first walls. In this analysis, we considered all sources of potential energy deposition to all these components including the original escaping plasma particles, radiation of the secondary generated plasma from the divertor material, and the deposition of the escaped core particles due to various scattering processes from the dense evolving secondary plasma plume. For clear demonstration of the investigated areas in ITER design, we magnified the divertor cassette zone illustrating the designated studied component surfaces as shown in Fig. 5. The inner (left side) and outer (right side) areas are also known as the high- and low-field areas. Lower parts of the Be first wall are designated as $\boxed{A}^{*}$ (inner) and $\boxed{B}^{*}$ (outer) walls (see Fig. 5). The divertor cassette component surfaces are numbered from $\boxed{1}^{*}$ to $\boxed{9}^{*}$ (see Fig. 5). The inner and outer baffle areas are designated as $\boxed{1}^{*}$ and $\boxed{2}^{*}$, respectively (see Fig. 5). The inner and outer divertor plates are designated as $\boxed{2}^{*}$ and $\boxed{8}^{*}$, respectively (see Fig. 5). The inner and outer stainless-steel tube structures are designated as $\boxed{4}^{*}$ and $\boxed{6}^{*}$, respectively (see Fig. 5). The dome structure is designated as $\boxed{5}^{*}$ (see Fig. 5). In Fig. 5, the origins and scale directions are shown with red arrows on the component surfaces. The component materials, i.e., Be, W, and SS, are illustrated with orange, blue, and teal colors, respectively. The black area shown in Fig. 5 corresponds to the core plasma bordered with dashed lines indicating the LCFS.

In this study, we investigated two types of plasma transient events, i.e., giant ELMs (total released plasma energy of 12.6 MJ) and major disruptions (of 126 MJ *in total energy*). Because of the uncertainties in the transient event duration, we have investigated four possible transient durations, i.e., 0.1, 0.5, 1.0, and 3.0 ms. The material of the secondary generated plasma was the current ITER divertor plate material made of tungsten. The response of the divertor plate surface to various transient events was excluded from this analysis since we have previously studied these in detail and no significant dispute exists about the expected damage in both the inner and outer divertor plates as a result of these plasma instability events.[5] As mentioned above, we used the quadtree mesh with four main levels in our MHD simulations. The minimum (4th) level cell size was ∼0.5 cm. However, for the subsurface processes, this 4th level was refined additionally to ∼0.5 μm. For the modeling energy deposition during the transient event, the Monte Carlo algorithm used ∼10^4 particles per one MHD time point, i.e., ten

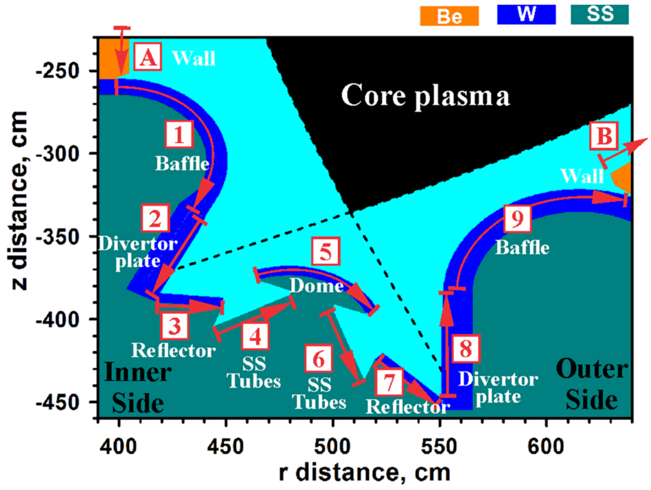

FIG. 5. ITER divertor space and the component surface designation*.

thousands particles are sampled on the LCFS every recalculation of the current core plasma flux and current energy deposition. The radiation transport calculations required sampling $\sim 10^4$ photons per each MHD cell. We used innovative weighted MC algorithms to reduce this number of photons, e.g., near vacuum and cold cells where photon emission is near zero to significantly decrease MC calculation time and to reduce errors and remove emission/absorption within cold cells. For photon radiation transport calculation, as mentioned early extensive atomic physics data were previously developed in HEIGHTS for various potential divertor materials (e.g., W, C, and Li) along with using the CRE model for calculating the evolving plasma characteristics. The photon generated energy spectra included up to 20 000 energy groups for each hydrodynamic cell within the evolving plasma to ensure accurate photon transport and energy deposition on various surrounding and nearby components.[9]

The escaped core plasma particles were determined the initial input energy source and boundary conditions for the MHD formation and evolution of the secondary divertor plasma. Initially, we assumed near vacuum conditions in the SOL for the secondary plasma: 10 Pa pressure and 500 K temperature, corresponding internal energy, and zero velocity. As we noted above, the equilibrium magnetic field was reconstructed from the EQDSK files. Conservation laws were maintained by calculating the energy and mass transport into the MHD domain above the receding surface after surface vaporization. Hydrodynamic conditions were set at the boundaries of the hydrodynamic domain and assume conditions of rigid walls for tokamak components and incoming/outgoing gas for the LCFS. The magnetic field conditions assumed conducting metallic walls. A more comprehensive discussion of the boundary condition used in HEIGHTS and their application is presented in Ref. 46.

The initially vaporized divertor material is continued to be heated and ionized by the incident escaping core plasma particles to higher plasma temperatures of tens of eV depending on the divertor material. This dense and ionized secondary plasma moves along the initial frozen magnetic field. This initial EQDSK poloidal and toroidal magnetic fields are changing and drifting with plasma expansion. Figure 6 shows the time-dependent change in poloidal magnetic field for the 0.1 ms disruption event [Fig. 6(a)] and the change in toroidal field for the 1.0 ms disruption event [Fig. 6(b)]. Near the strike point area is the most dense secondary plasma formation. The coordinate origin shown in Fig. 6 is placed at the outer strike point and the calculated magnetic fields are shown in the direction S′ normal to the divertor plate. As shown in Fig. 3(b), the direction S′ is in the opposite direction to the r-axis of the reactor and the radial component of magnetic field B_r is to illustrate the motion of the frozen magnetic field lines during the disruption. The green line is the initial equilibrium magnetic field in this area. The convective processes of plasma motion accelerate the movement of the frozen magnetic field lines, while the dissipative magnetic diffusion processes have the opposite effect. The magnetic diffusion tends to smooth the resulting gradients and seeks to return to the initial field distribution. These processes are both time- and space-dependent on transient event parameters. Figure 6(b) shows the change in the toroidal field component during the 1.0 ms disruption.

HEIGHTS simulation of the full 3-D ITER configuration including the divertor cassette, various nearby components, and the first walls calculates in detail the temperature and thermal response of each component at each point on the surface during the entire duration of these events from all potential heating sources. We previously studied in detail the secondary plasma parameters, e.g., plasma temperatures and densities for both W and C as PFCs and the resulting surface damage for various disruption and ELM parameters.[9] The first step of our study was to calculate the time-temperature history for all surfaces regardless of identifying which specific heating source is the main contributing source, i.e., secondary plasma radiation or scattered/reflected incident core plasma particles. Additionally, the temporal maximum temperature history is recorded regardless of which specific

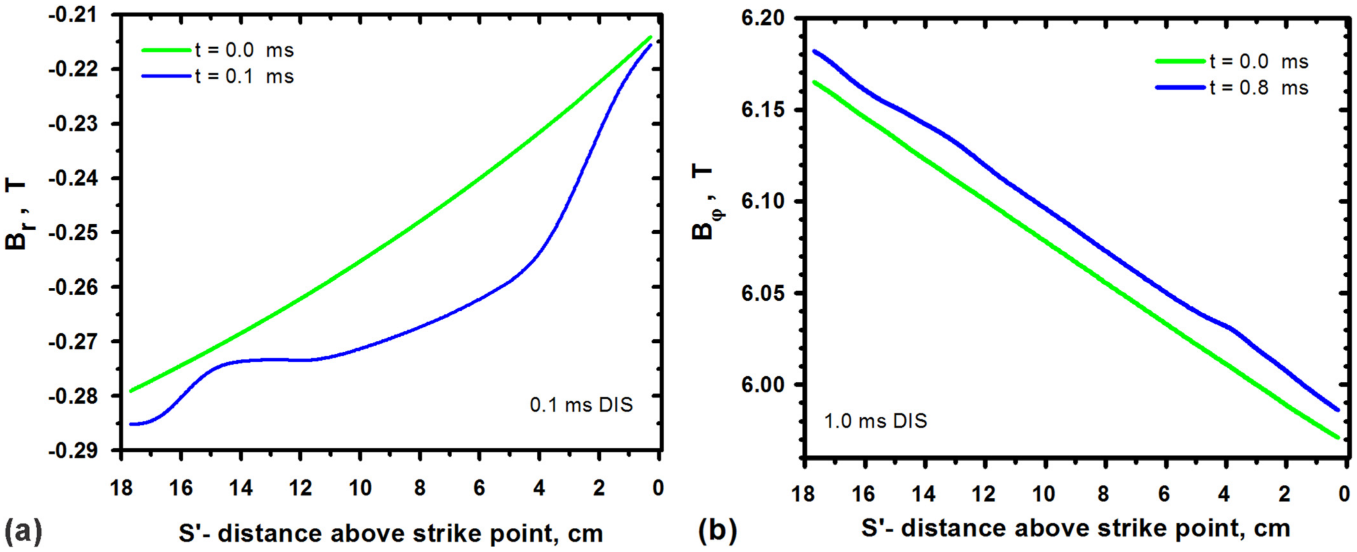

FIG. 6. Magnetic fields drift during secondary plasma evolution for (a) 0.1 ms disruption and (b) 1.0 ms disruption.

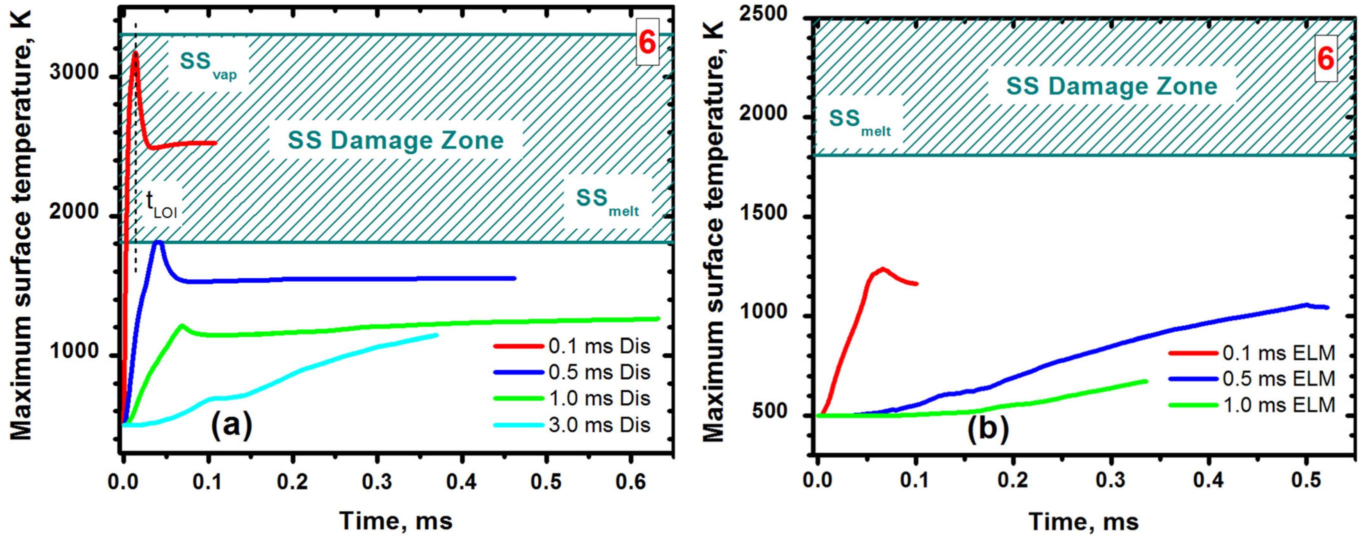

FIG. 7. The time-temperature curves of the dome stainless steel outer tube surface $\boxed{6}^{*}$ (see Fig. 5) during the (a) disruption event and (b) ELM event.

location on the selected surface is reaching the maximum temperature calculated. These locations vary dynamically as the secondary divertor plasma evolves and propagates through the SOL and interacts with the incoming disrupting plasma particles. These calculations identify potential problem-causing areas and the critical time moments during the simulating events. Figure 7 confirms our previous modeling results where we studied the secondary radiation potential damage to the open stainless-steel dome tubes.[10] We hatched in Fig. 7 the damage zone as the area above the melting point for the SS material $T_{melt}^{SS} = 1810\,\mathrm{K}$. The curves shown are not specific to a certain point at the dome surface but illustrate the maximum temperature reached on these surfaces during these events. The analysis shown in Fig. 7 demonstrates the expected decrease in heat loads to the SS tube structure with the time duration of the transient event. The dependence can be explained assuming that the source of the energy deposition is mainly the secondary radiation and effective energy deposition is achieved when the dense plasma cloud is close to the SS tube structure. The shorter high-power event initiates an intense secondary plasma plume near the SS tubes.

To confirm this, the radiation and particle fluxes were calculated along the outer SS tube at time moment of this hot spot location (L_{HS}), i.e., time of the highest surface temperature achieved for this component and conditions at this L_{HS}, marked in Fig. 7(a): $t_{HS} = 14\ \mu s$ during the 0.1 ms disruption. Figure 8 indicates the spatial distribution of radiation flux input correlated with the temperature distribution of the SS tube inner and outer surfaces. The umbrella tubes in this case are only overheated due to the radiation from the secondary divertor plasma. The particle flux is equal to zero in both cases and is not shown in figures. These data are in good agreement with our previous calculations[10] and can be considered an additional benchmarking of the extensive revised full 3-D model and detailed geometrical configuration.

Contrary to the situation on the SS tube surfaces where the radiation flux dominates the total input heat source, is the

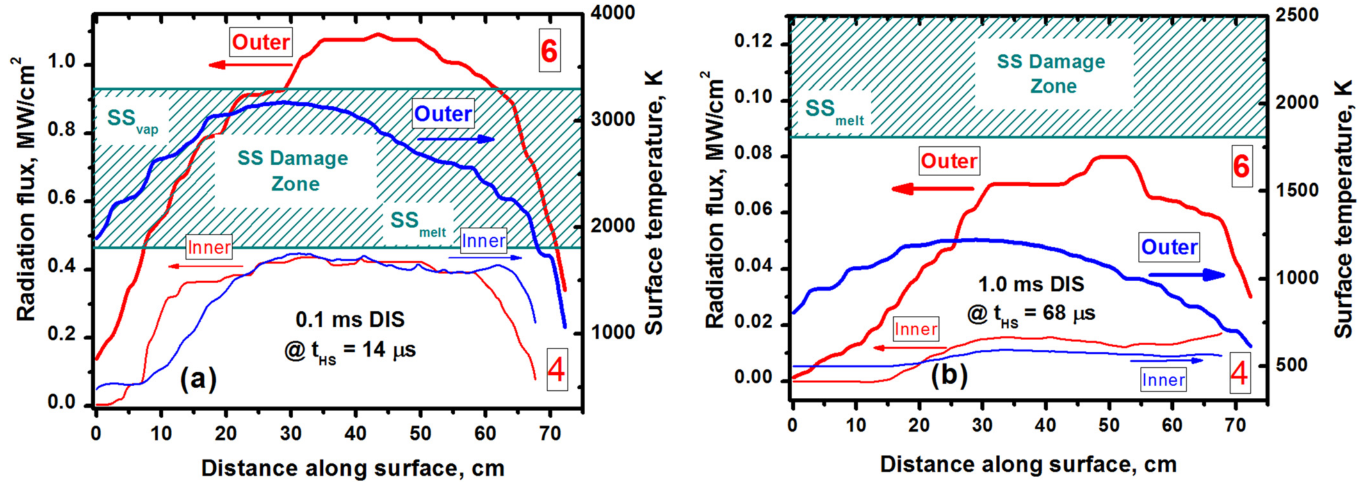

FIG. 8. The radiation flux and temperature distributions along the stainless-steel inner $\boxed{4}^{*}$ and outer $\boxed{6}^{*}$ tubes at the time of the maximum temperature (see Fig. 5): (a) 0.1 ms disruption case and (b) 1.0 ms disruption case. The particle flux is equal to zero in these cases and is not shown. Left arrows correspond to radiation flux and right arrows to surface temperature.

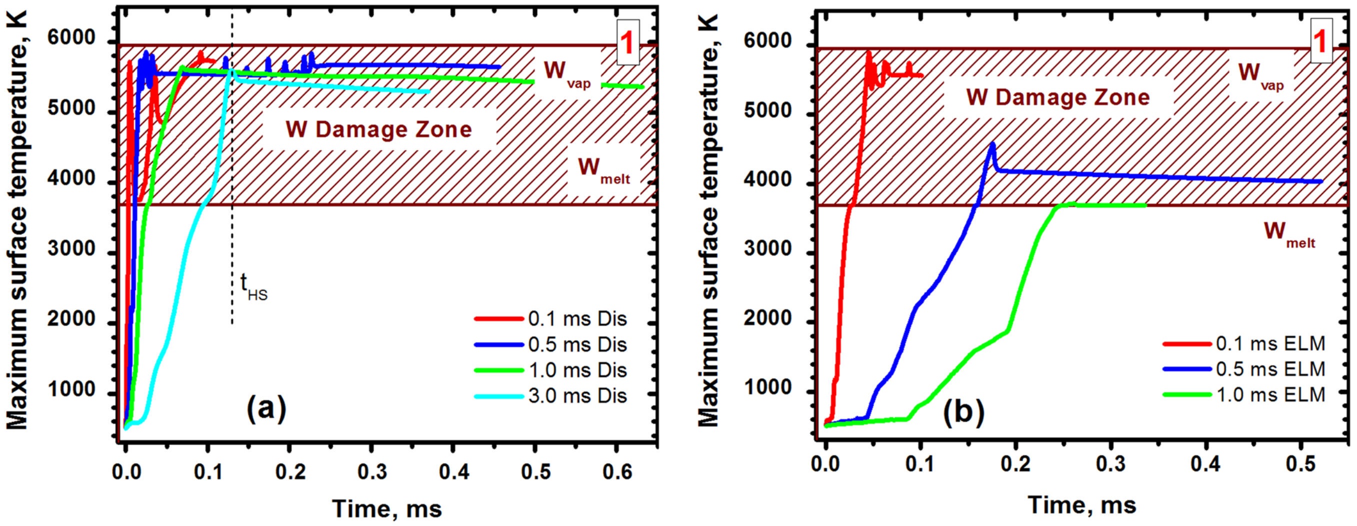

FIG. 9. The time-temperature curves of the inner Baffle surface $\boxed{1}^*$ (see Fig. 5) during (a) disruption and (b) ELM.

baffle surfaces which are located much farther from the original disruption location at the strike points and the initially evolving secondary plasma plume. The plasma cloud takes time to propagate and drift to the baffle while still interacting with the incident main disrupting plasma particles. The secondary plasma during the drift and propagation in the poloidal plane continuously interacts with the incident shower of the escaped core plasma particles. These escaped particles undergo various collisional and scattering processes with the expanding plasma cloud. The scattered ionized particles can change the current magnetic field line path (see Fig. 3) and when closer to component surfaces can cause intense local deposition, i.e., "hot spots" on the component surface.

The described processes are dynamical due to the plasma cloud motion, propagation through the SOL, and magnetic field diffusion and therefore, the hot spots should have a dynamic character depending on plasma cloud particle density and temperature distributions, disrupting core plasma particles, magnetic field, and the geometrical location of components. Figure 9 shows, for example, a typical time history for the inner, i.e., high-field (HF) Baffle surface (i.e., zone $\boxed{1}^*$, Fig. 5) for different disruption and ELM time durations. Contrary to the SS tube case, the baffle temporal response is more dynamical and can have several spots of maximum temperature corresponding to various secondary plasma spatial locations and characteristics.

Figure 10 shows the spatial distributions of the deposited power flux and the temperature rise at the hot spot location L_{HS} time moment ($t_{HS} = 130\,\mu s$), for the 3.0 ms disruption case marked in Fig. 9, where the maxiumum temperature is reached. As predicted, the radiation flux is very small compared to the particle flux since the secondary plasma cloud is not yet close enough to the baffle location but the scattered particle flux is capable of heating local spots on the baffle surface. The scattering processes are dynamical and the hot spot locations are mobile, the peak of the particles power flux is shifted relative to the maximum temperature location.

The resulting localized hot spots can further be initial sources of transient spot melting and potential splashing and contamination problem that are currently being actively studied by the fusion community.[47] The contribution of the

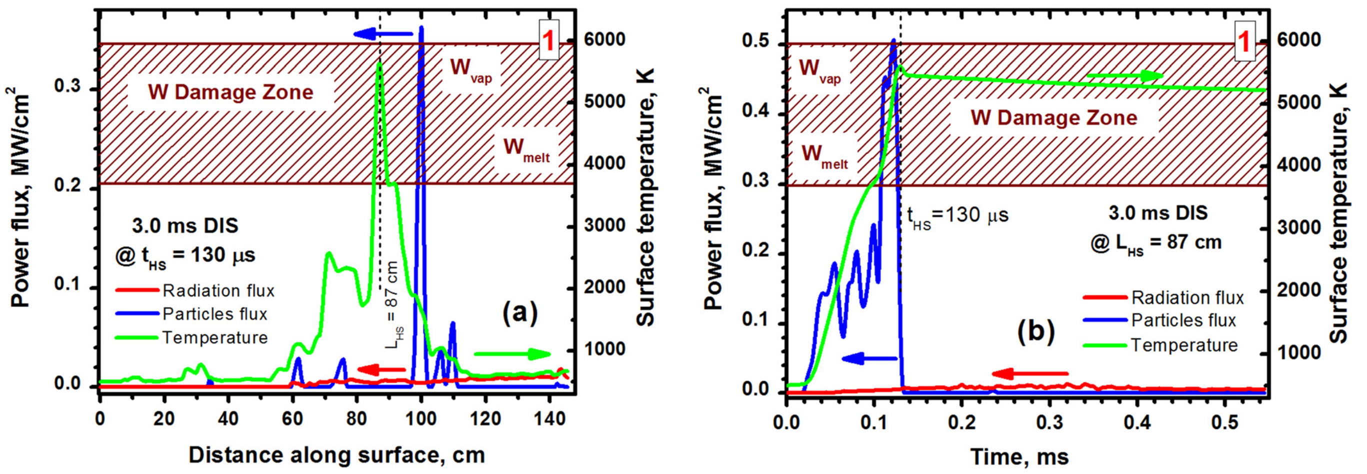

FIG. 10. Spatial distribution along the inner Baffle surface $\boxed{1}^*$ (see Fig. 5) (a) and temporal distribution (b) of the particle and radiation power fluxes and the resulting surface temperature.

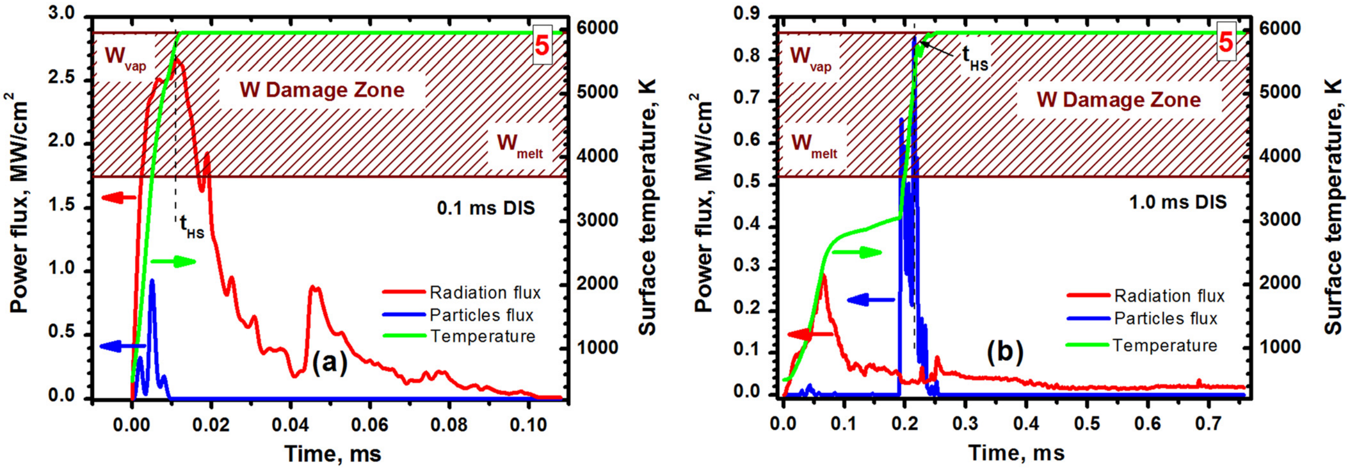

FIG. 11. Distribution along the W Dome surface $\boxed{5}^*$ (see Fig. 5) during (a) 0.1 ms disruption and (b) 1.0 ms disruption.

particle flux and the secondary radiation input to various plasma facing and nearby components depend on the dynamics of the evolving plasma and its spatial location. Initially, the particle flux on the original disruption location at the strike point on the divertor plate is the main energy source to initiate the secondary plasma of the divertor plate material. The incident and the scattered particle flux from the initiated dense cloud continues to mainly heat the secondary cloud and causes ionization and plasma formation. This happens regularly and closer to the beginning of the transient event when the secondary plasma is already initiated and acts as a target for scattering but did not evolve or expand up to the total shielding size. The radiation power flux starts to significantly contribute after the full shielding and the formation of the hot dense radiative plasma cloud. The radiation flux input of the secondary plasma is a complex function of transient event power, duration, divertor material, and divertor geometrical design. A shorter disruption time event will quickly initiate a dense hot secondary plasma cloud that can damage various nearby surfaces. In a longer transient event, the secondary radiation resulting damage will be delayed since the plasma plume requires more time to be formed and moved closer to the component surfaces. In most cases, the heated and damaged areas due to radiation fluxes were wider than the hot spots resulting from the scattered particles flux.

To define the main energy source of the resulting damage, three flux and temperature time histories were plotted for the same surface, i.e., maximum particle flux, maximum radiation flux, and maximum temperature. These three values can, however, be related to different locations on the same surface. Figure 11 shows typical situations for a short (0.1 ms) and a long (1.0 ms) disruption where either the radiation flux or particle flux dominates correspondingly. In both cases, surface vaporization occurred on the dome surface but in the case of the shorter 0.1 ms disruption [Fig. 11(a)], a much higher radiation flux rapidly heated the dome surface, while in the longer 1.0 disruption case [Fig. 11(b)], a much higher localized particle flux deposited more energy into the radiation pre-heated surface location.

To illustrate how the radiation or particles energy fluxes arrive at the component surface, we reconstructed the radiation and particle fluxes, for example, near the dome surface [i.e., surface $\boxed{5}^*$ (see Fig. 5)]. Based on the secondary plasma density and temperature, the radiation fluxes were calculated for the case of the shorter 0.1 ms disruption at the time moment $t_{HS} = 11\ \mu s$ [See the time moment in Fig. 11(a)]. As

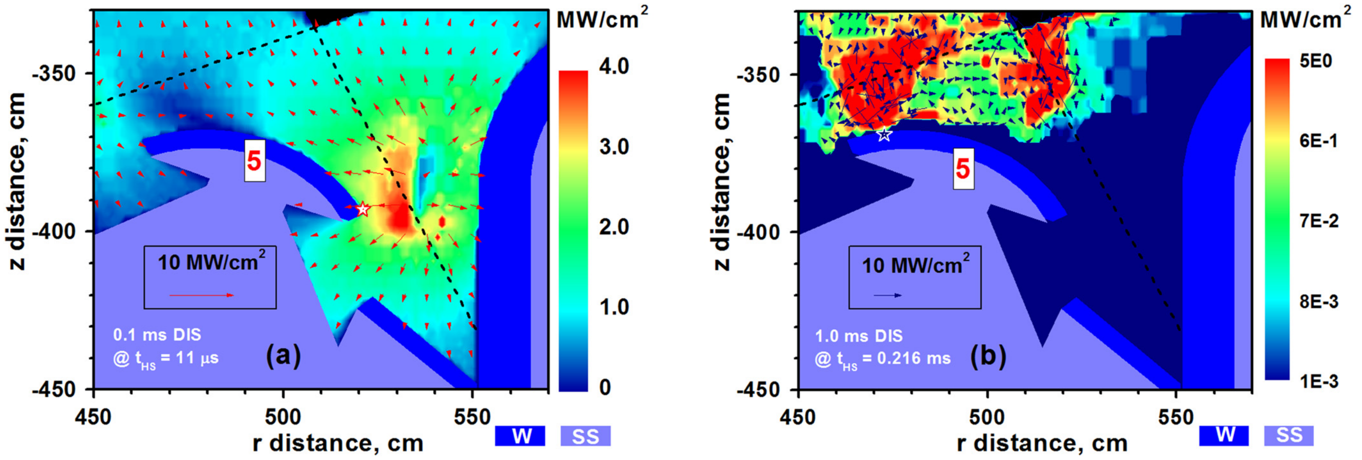

FIG. 12. Tungsten Dome surface $\boxed{5}^*$ (see Fig. 5) damage caused mainly by: (a) photon radiation during the shorter 0.1 ms event (disruption) and (b) scattering of disrupting core particles during the longer 1.0 ms event.

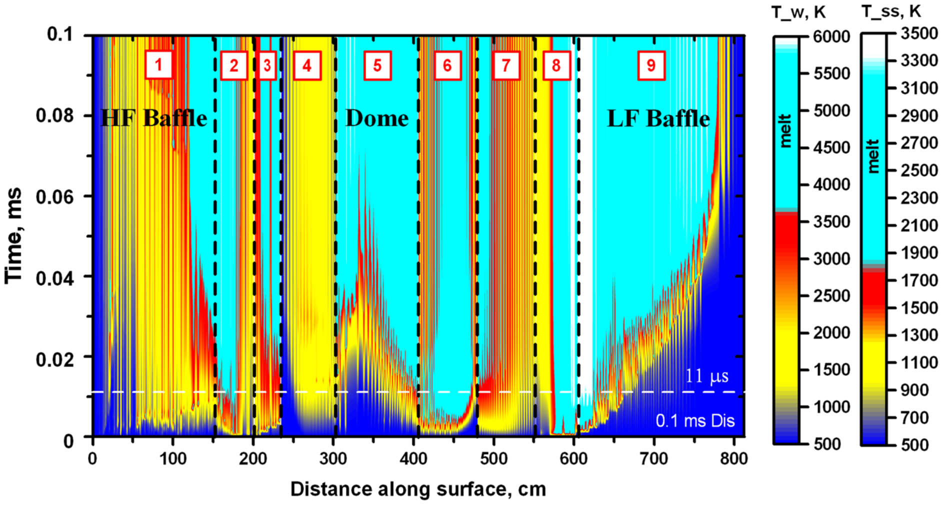

FIG. 13. Thermal response of divertor zone surfaces during 0.1 ms disruption.

shown in Fig. 12(a), the secondary plasma plume and the radiation source arrived near the edge of the dome. The melted surface location (marked by red star) is the closest to the radiation source area. Figure 12(b) shows the case of the longer event (1.0 ms disruption) and the energy deposition produced mainly by the scattered particle flux. Up to the LOI moment $t_{HS} = 0.216$ ms [See the time moment in Fig. 11(b)], the plume is then sufficiently developed so the bottom divertor space is fully shielded by the secondary plasma. The escaped core particles cannot penetrate and reach the divertor plate surfaces. It is very important to take into account the details of the gyrating motion of particles especially when the Larmor radius is comparable with the cell size and the particle enters and exits the computational cell many times. HEIGHTS implements the operable algorithm for that and Fig. 12(b) shows the scattering drift of the escaped core particles at the time moment $t_{HS} = 0.216$ ms. As shown in the figure, the damaged spot on the dome surface (marked by a blue star) clearly corresponds to the particle flux on the dome surface.

Note however that the scattering of the escaped core plasma particles from the expanding secondary divertor plasma, e.g., Fig. 12(b), is not a fully chaotic process and not any random surface/location could be exposed and damaged. Instead, the scattering and deposition areas are fully determined and controlled by the expanding and the heating of the secondary plasma plume, various collisional and scattering processes and cross sections, and very specific time-dependent magnetic configuration, and component design. These are self-consistent processes, e.g., particle deposition influences plasma motion and plasma configuration and characteristics determine the scattering processes and deposition areas.

As an example, to show the response of all cassette components during a single transient event, Fig. 13 illustrates the temporal-spatial map of the surface temperature of all components [i.e., $\boxed{1}^*$–$\boxed{9}^*$ (see Fig. 5)] for the shorter disruption time of 0.1 ms. All these components are made of either tungsten (baffle, divertor plate, reflector, and dome) or stainless steel (umbrella tubes). In this figure, all surfaces are combined along one spatial line starting from the beginning of the inner baffle up to the end of the outer baffle and are marked correspondingly to the previously defined configuration in Fig. 5. The vertical time axis is shown to flow from the bottom to top where the hot spot time point $t_{HS} = 11\ \mu s$ is shown as the white horizontal dashed line. At the right side of the figure, two color bars show the magnitude of temperature rise for the tungsten and stainless steel component structure. We excluded beryllium walls in this figure for simplicity. The cyan color denotes melting of the metal and white color indicates vaporization. It can be seen that large surfaces of the divertor components are melted and some spots are even vaporized. Figure 13 does not indicate the specific surface heating source for the resulting damage (i.e., escaped core particles, scattered particles, or secondary plasma radiation) but illustrates the predicted dynamic damage profile for the shortest transient disruption event of 0.1 ms.

The blue color of the left and right sides of Fig. 13 indicates no serious damage of the tungsten edges of the Inner and Outer Baffles $\boxed{1}^*$ and $\boxed{9}^*$ (see Fig. 5) during the duration of the short disruption event. The secondary plasma requires more time to arrive in remote areas. However, the beryllium first wall surfaces can melt depending on the secondary plasma dynamics. The Inner Wall $\boxed{A}^*$ (see Fig. 5) surface is better protected in the current ITER design and magnetic configuration than the Outer Wall $\boxed{B}^*$ (see Fig. 5). In fact, our simulations predicted damage to the Outer Be Wall $\boxed{B}^*$ (see Fig. 5) during disruptions of any duration considered in this analysis as shown in Fig. 14. Significant melting occurs over substantial areas of the Outer Be Wall that extends more than one meter long. This is a very serious problem and can only be predicted through comprehensive integrated simulation in full 3D realistic reactor geometry. The 3.0 ms disruption case is not shown since the simulation is not finished yet and has been continuously running for several months on ANL supercomputer clusters.

In addition to the serious concern of hidden and nearby component vaporization, the melting thicknesses and its spatial profiles are important for potential melt splashing and plasma contamination. For example, recent TEXTOR experiments have shown fine melt spray and macroscopic losses of tungsten melt in the form of fine spray with continuous ligaments and large droplets.[48] Figure 15 shows another example

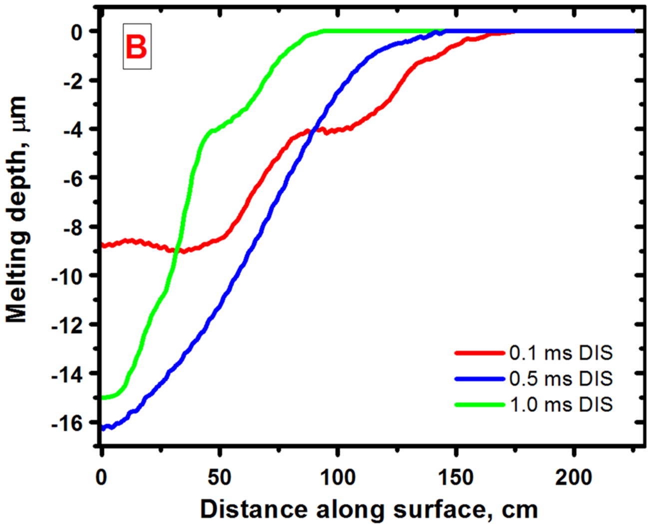

FIG. 14. Melting spatial profiles of the Outer beryllium Wall $\boxed{B}^*$ (see Fig. 5) directly after or near the end of the disruption event of various durations.

of the spatial melt profiles of the Dome $\boxed{5}^*$ and both Baffles $\boxed{1}^*$, $\boxed{9}^*$ (see Fig. 5) at two different time moments during the 1.0 disruption. Significant melting over substantial areas of these components can take place during such transient events.

After the analysis of various time dependent component responses (similar to those presented in Figs. 7 and 9), we have constructed Table I that summarizes the results of the main surface damage mechanisms, i.e., either secondary plasma radiation (R), or scattered particle flux (P), or both (P + R). Table I data confirm clearly our previous concerns and predictions regarding the high damage risk of divertor nearby component surfaces due to indirect heat loading factors, i.e., radiation of the produced divertor mini plasma and the scattering of incident core particle flux due to the interaction with the evolving dense mini plasmas. HEIGHTS simulation results showed the strong dependence of the surface damage on the geometrical design and magnetic configuration of the divertor zone. For example, it was anticipated that the most critical area for damage is the baffle surfaces but it was not anticipated that damage could occur on the inner Be first wall ($\boxed{A}^*$, see Fig. 5). We should however emphasize that the calculation is still in progress for the case of 1.0 ms disruption (now 70% complete) and for the 3.0 ms disruption (only 20% complete) up to this moment [Fig. 9(a)] and the secondary plasma cloud and its radiation are not fully arrived to the walls A and B yet. Table I summarizes the comparison of the contribution of the two secondary damage sources indicating which source is more frequent, more effective, and which surfaces are expected to be damaged or at potential risk of being damaged. For this purpose, we have simulated all cases presented for various disruption and ELMs time. The maximum particle fluxes and the maximum surface temperatures of each component were used to fill Table I with the identified main damage source. For example, Fig. 11(a) shows the damage mechanism that can be characterized as an input of particles (P) and main large input of the radiation (R). We marked this source as (R + P). Here, the capital letter is assumed for a flux value of higher than 0.5 MW/cm^2. As an example, Fig. 11(b) can be then be marked as (r + P) corresponding to these notations.

In general, during the transient events the outer divertor plate is exposed to twice the heat load of the inner side divertor plate. However, the initiated and expanding secondary plasmas, from each of the divertor plates, redistribute the energy deposition of the incoming disrupting plasma particles. Therefore, the resulting damage of the inner and outer components will depend on such interactions as well as on the geometrical configurations of the inner and outer areas. For example, as shown in Table I, the outer Reflector surface has much less damage in comparison to the inner side Reflector. However, there is an opposite situation with the outer and inner side SS Dome Tubes structure. The inner Dome Tubes has less potential damage. To mitigate such damage and to distribute the heat load more efficiently and to redirect the drift of the secondary plasmas in divertor space, the component design and magnetic configuration should be further optimized. We used brackets in Table I:

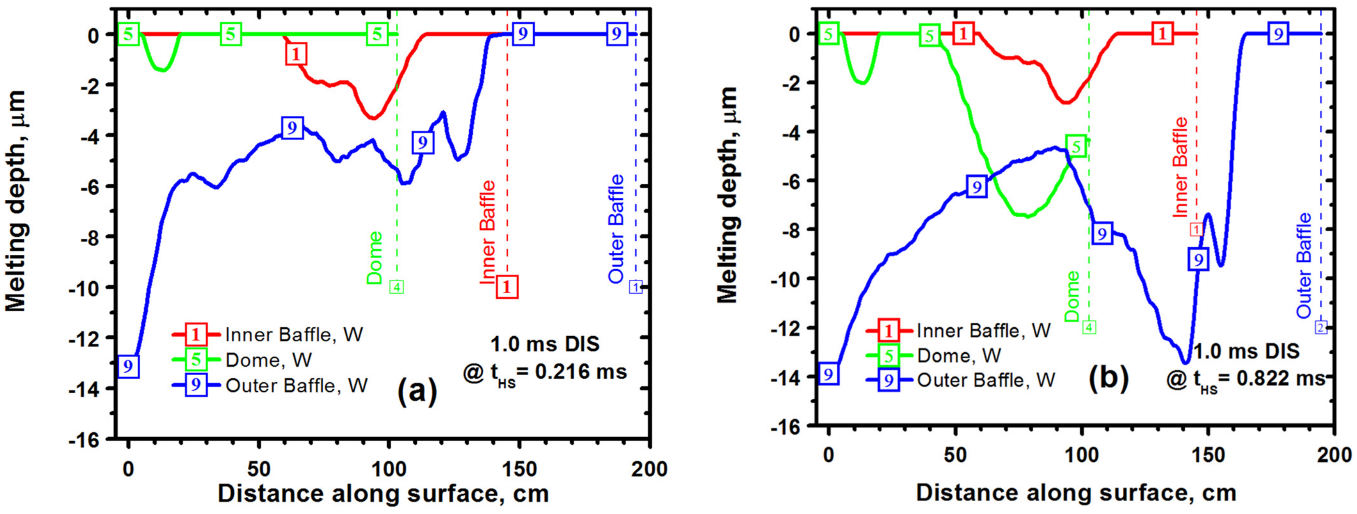

FIG. 15. Melting spatial profiles of tungsten Inner/Outer Baffles and Dome surfaces during the 1.0 disruption at time moments: (a) 0.216 ms and (b) 0.822 ms. Vertical dashed lines indicate the end of surfaces.

TABLE I. HEIGHTS predictions of damage map of ITER surfaces during transient events: {braces}—vaporization damage; [square brackets]—melting damage; no brackets—no damage is expected. Indexes: p–particles, r–radiation.

	Duration, ms	$\boxed{A}$ Inner wall **Be**	$\boxed{1}$ Inner baffle **W**	$\boxed{2}$ Inner divertor plate **W**	$\boxed{3}$ Inner reflector **W**	$\boxed{4}$ Inner tubes **SS**	$\boxed{5}$ Dome **W**	$\boxed{6}$ Outer tubes **SS**	$\boxed{7}$ Outer reflector **W**	$\boxed{8}$ Outer divertor plate **W**	$\boxed{9}$ Outer baffle **W**	$\boxed{B}$ Outer wall **Be**
DIS	0.1	p+r	{P+R}	{P+R}	{P+R}	{P+r}	{R+P}	{R}	[R]	{P+R}	{P+R}	{R}
	0.5	r	{P+r}	{P+R}	{P+r}	r	{R+P}	[r]	r	{P+R}	{P+R}	{r+P}
	1.0	r	{P}	{P}	{P}	r	{r+P}	r	p+r	{P+r}	{P+r}	{r+P}
	3.0	p+r	{P}	{P+r}	[p]	r	[r+p]	r	r	{P}	{P+r}	r
ELM	0.1	p+r	{P}	{P}	[P]	r	r	r	r+p	{P+r}	{P+r}	r
	0.5	p+r	[p]	{P}	[p]	r	p+r	r	r	{P}	[p+r]	r
	1.0	p+r	[p]	{p}	[p]	r	p+r	r	p+r	{p}	p+r	r

braces for vaporization damage and square brackets for melting damage. The 3.0 ms disruption case is not yet finished and for now we did not use brackets for the Outer Wall $\boxed{B}^*$ (see Fig. 5). However, we predict square brackets for this cell to the end of disruption event.

The computation requirements are tremendous, including full 3-D real ITER geometry with a magnetic field dynamic structure, millions of hydrodynamic cells, millions of photons in each cell, thousands of incident D, T, and electron particles, extensive atomic physics and very fine energy groups for photon emission and absorption of photon transport, and component geometry sizes vary from meters to submicron level zones. The accuracy of these calculations could be even improved further by increasing the number of particles and photons, by reducing the size of hydrodynamic cells, and by increasing the opacity and emissivity energy spectral groups in the secondary plasma. We used for our current simulations the Bebop cluster at the Argonne National Laboratory, one of the world fastest computers, based on the Intel Xeon E5-2695v4 processors with memory 128 Mb per node with a peak capability of 1.5 petaflops.[49] Despite that, the current version of HEIGHTS package takes many months to complete just one single case of the transient event using the full 3-D integrated model with real ITER geometry. Further acceleration of HEIGHTS through efficient parallelization, particularly of the MHD package, is urgently needed to significantly reduce the execution time of such challenging integrated calculations. We have also briefly compared the difference in the nearby component response if the original divertor plates were made of C instead of W. All other components and design configurations are assumed the same. Of course, we are also aware of the other problems of having the divertor plate made out of C instead of W. However, C generated divertor secondary plasma as a result of plasma instabilities, being a low z-material, will have much lower radiation in the divertor areas compared to W.

Figure 16 shows a comparison between the response of the inner divertor plates [C-Fig. 16(a) and W-Fig. 16(b)], inner W reflector plate, inner SS tube structure, and the W dome. The calculation shown is for 0.1 ms full disruption event. The figure clearly shows that using C as the divertor plate will protect nearby components such as the reflector plates, the SS tube structure, and the dome much better than a W divertor plate for the parameters studied in this case. In fact, no potential melting or vaporization of all these components occurs compared to the case of the W divertor plate in which these three components would be damaged. However, the response of these components and others for different disruption parameters and conditions could be different if the

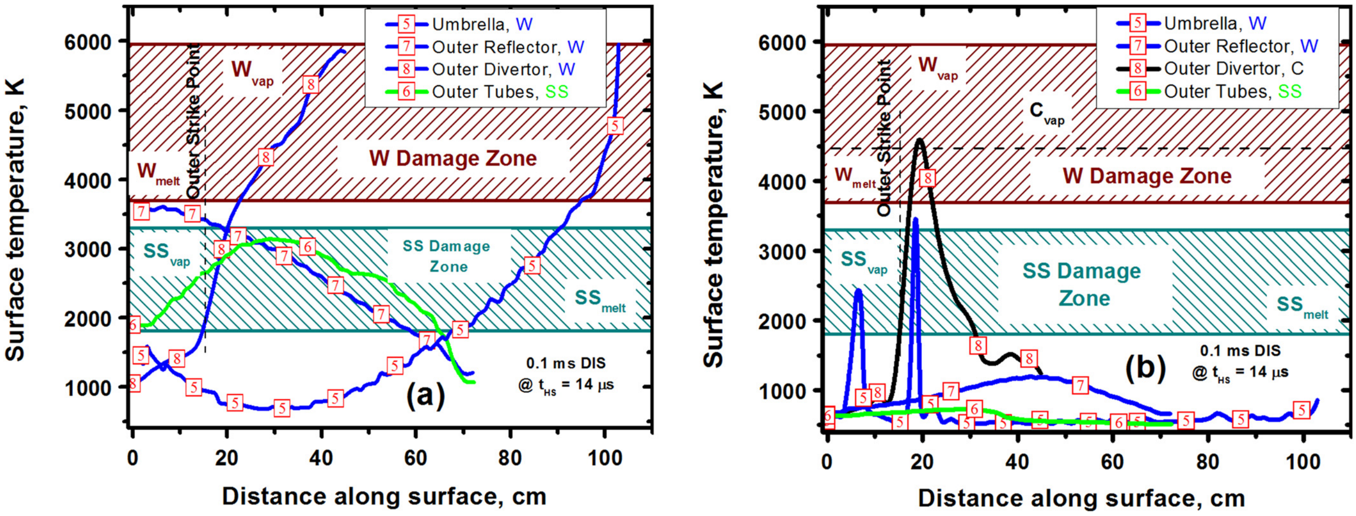

FIG. 16. Response of nearby components [outer reflector $\boxed{7}^*$, outer SS Tube $\boxed{6}^*$, Dome $\boxed{5}^*$ (see Fig. 5)] for different divertor plate materials: (a) W divertor $\boxed{2}^*$, $\boxed{8}^*$; and (b) C divertor $\boxed{2}^*$, $\boxed{8}^*$ (see Fig. 5).

divertor plates were made of C instead of W. In addition, the hot-generated less-radiative C plasma may travel farther and damage other components. In summary, analysis of various mitigation and innovative methods to protect the internal components must be studied in detail using full 3-D integrated realistic geometry and design features. These should include pellet injection, massive gas puffing, innovative materials, better design innovation, use of liquid metals, etc. Currently, the ITER design configuration may not be durable to accommodate and survive a single unmitigated major plasma instability event. This should be taken very seriously and investigated in detail since it has great implication for the success of the tokamak concept and in particular ITER current design as future energy producing devices.

IV. CONCLUSIONS

The HEIGHTS simulation package, over the years, has been successfully benchmarked in current tokamaks and in powerful plasma gun devices worldwide for fusion and other high power applications such as laser and discharge produced plasma devices, nanolithography, and particle accelerators.[7,10,38,50,51] The procedure of benchmarking HEIGHTS models and computer package included both individual validations of each separate computational block and components and benchmarking the whole integrated package against available experimental and theoretical data. Recently, we have significantly upgraded HEIGHTS to build on the enhancement of numerical and computational methods as well as the physics and strive to continue as the leading tool for modeling the integrated 3-D reactor component response during various transient events and assess potential damage mechanisms to every internal component of the cassette structure as well as the first walls. In this study, we analyzed, for the first time, in fine geometrical and physics detail the integrated effects of various transient events with a wide range of parameters that are relevant to ITER design. During these events, the disrupting plasma particle energy is converted to two significant secondary heat sources that can cause serious damage to internal and hidden components that were not directly exposed to disruptions and ELMs. These two major sources are photon radiation of the secondary generated plasmas from the inner and outer divertor plates as well as the scattered incident disrupting plasma particles from the evolving secondary plasmas. The collisions of the incident core particles with secondary plasma and the deflected/scattered energetic particles under the strong magnetic field structure can lead to significant energy transfer to nearby component surfaces. The scattered energetic particles can also jump across the evolving magnetic field lines and deposit its energy in various surrounding structures depending on the expanding plasma cloud characteristics and location. We find that the scattered particles jump across the magnetic field lines and drift in the poloidal tokamak cross-section during the toroidal motion and can produce intense local heat loading, i.e., hot spots far from the divertor plates and from the original strike points. The local heat loading in these hot spots areas is time-dependent due to the self-consistent character of the core plasma – secondary plasma interaction and motion during the course of the transient events. Our simulations of the current ITER design highlighted the surfaces that can be significantly damaged during the transient events due to particles and/or secondary radiation fluxes. We also identified areas on various component surfaces where the scattered particle flux can further damage preheated spots due to photon radiation from the divertor-generated plasma cloud. HEIGHTS also predicted unexpected damage to the Be first walls as a result of transient events on the divertor plates. It is, therefore, concluded that the details of the collisional and radiative processes in the divertor region and the dynamic magnetic configuration are critically important to evaluate the response of all cassette components and greatly depend on the dynamics of the evolving secondary divertor plasmas.

In summary, our comprehensive results show, for the first time, that transient events, including even those with longer durations, could cause significant melting and vaporization damage to most interior and hidden plasma-facing and related components, including the first walls that were not directly exposed to the original disrupting plasma particles. These hidden interior components will be hard to repair in a timely matter and could potentially shut down the reactor operation for extended periods of time. One may not be able to successfully operate ITER after just a single transient event. The current ITER divertor design may need to be modified or new design may be needed to prevent this damage. For example, in addition to the liquid metal options which may be is harder to implement in ITER at this stage, the snowflake-like configuration could be a good geometrical solution to reduce heat loads onto material surfaces and to redirect the secondary plasmas away from nearby components. Diverted configurations could significantly reduce the interaction of the resulting divertor plasma with nearby components due to the strike points being situated at much longer distances from the evolving hot and dense plasma.[52,53]

SUPPLEMENTARY MATERIAL

See supplementary material for the combined temperature-density evolution of the secondary plasma during the 0.1 ms disruption can be illustrated in the attached Movie1_0.1Dis_DenTemp.flv. In Movie 1, the temperature is plotted in color fields and density is indicated with contour lines. The damaged surface areas can be seen by the density evolution of these components as shown in Movie2_0.1Dis_Den.flv where secondary plasma density is plotted in color.

ACKNOWLEDGMENTS

We gratefully acknowledge the computing resources provided by the Bebop cluster operated by the Laboratory Computing Resource Center at Argonne National Laboratory. This work was partially supported by the National Science Foundation.

[1] L. Schmitz, Nucl. Fusion **57**, 025003 (2017).
[2] T. Eich, A. W. Leonard, R. A. Pitts, W. Fundamenski, R. J. Goldston, T. K. Gray, A. Herrmann, A. Kirk, A. Kallenbach, O. Kardaun, A. S. Kukushkin, B. LaBombard, R. Maingi, M. A. Makowski, A. Scarabosio,

B. Sieglin, J. Terry, and A. Thornton, ASDEX Upgrade Team and JET EFDA Contributors. Nucl. Fusion **53**, 093031 (2013).

[3] K. Ikeda, Nucl. Fusion **47**, S1 (2007).

[4] G. Federici, P. Andrew, P. Barabaschi, J. Brooks, R. Doerner, A. Geier, A. Herrmann, G. Janeschitz, K. Krieger, A. Kukushkin, A. Loarte, R. Neu, G. Saibene, M. Shimada, G. Strohmayer, and M. Sugihara, J. Nucl. Mater. **313–316**, 11 (2003).

[5] V. Sizyuk and A. Hassanein, Nucl. Fusion **50**, 115004 (2010).

[6] A. S. Kukushkin, G. Janeschitz, A. Loarte, H. D. Pacher, D. Coster, D. Reiter, and R. Schneider, J. Nucl. Mater. **290–293**, 887 (2001).

[7] V. Sizyuk and A. Hassanein, J. Nucl. Mater. **438**, S809 (2013).

[8] A. Widdowson, S. Brezinsek, J. P. Coad, D. E. Hole, J. Likonen, V. Philipps, M. Rubel, and M. F. Stamp, and JET-EFDA Contributors. Phys. Scr. **T138**, 014005 (2009).

[9] V. Sizyuk and A. Hassanein, Phys. Plasmas **22**, 013301 (2015).

[10] V. Sizyuk and A. Hassanein, Nucl. Fusion **53**, 073023 (2013).

[11] L. Guimarais, S. Potzel, C. Silva, M. Bernert, D. Carralero, G. D. Conway, L. Gil, M. E. Manso, V. Nikolaeva, F. Reimold, J. Santos, A. Silva, U. Stroth, J. Vicente, M. Wischmeier, E. Wolfrum, The ASDEX Upgrade Team, and The EUROfusion MST1 Team, Nucl. Fusion **58**, 026005 (2018).

[12] R. Maurizio, S. Elmore, N. Fedorczak, A. Gallo, H. Reimerdes, B. Labit, C. Theiler, C. K. Tsui, W. A. J. Vijvers, The TCV Team, and The MST1 Team, Nucl. Fusion **58**, 016052 (2018).

[13] T. E. Evans, I. Joseph, R. A. Moyer, M. E. Fenstermacher, C. J. Lasnier, and L. W. Yan, J. Nucl. Mater. **363–365**, 570 (2007).

[14] O. Schmitz, M. W. Jakubowski, H. Frerichs, D. Harting, M. Lehnen, B. Unterberg, S. S. Abduallaev, S. Brezinsek, I. Classen, T. Evans, Y. Feng, K. H. Finken, M. Kantor, D. Reiter, U. Samm, B. Schweer, G. Sergienko, G. W. Spakman, M. Tokar, E. Uzgel, R. C. Wolf, and the TEXTOR Team, Nucl. Fusion **48**, 024009 (2008).

[15] M. W. Jakubowski, T. E. Evans, M. E. Fenstermacher, M. Groth, C. J. Lasnier, A. W. Leonard, O. Schmitz, J. G. Watkins, T. Eich, W. Fundamenski, R. A. Moyer, R. C. Wolf, L. B. Baylor, J. A. Boedo, K. H. Burrell, H. Frerichs, J. S. deGrassie, P. Gohil, I. Joseph, S. Mordijck, M. Lehnen, C. C. Petty, R. I. Pinsker, D. Reiter, T. L. Rhodes, U. Samm, M. J. Schaffer, P. B. Snyder, H. Stoschus, T. Osborne, B. Unterberg, E. Unterberg, and W. P. West, Nucl. Fusion **49**, 095013 (2009).

[16] W. Guttenfelder, A. R. Field, I. Lupelli, T. Tala, S. M. Kaye, Y. Ren, and W. M. Solomon, Nucl. Fusion **57**, 056022 (2017).

[17] V. Rozhansky, E. Kaveeva, and M. Tendler, Plasma Phys. Controllled Fusion **57**, 115007 (2015).

[18] H. Du, C. Sang, L. Wang, X. Bonnin, H. Wang, J. Sun, and D. Wang, Nucl. Fusion **57**, 116022 (2017).

[19] D. P. Stotler, R. Maingi, L. E. Zakharov, H. W. Kugel, A. Y. Pigarov, T. D. Rognlien, and V. A. Soukhanovskii, Contrib. Plasma Phys. **50**, 368 (2010).

[20] T. D. Rognlien, R. H. Bulmer, M. E. Rensink, and J. N. Brooks, J. Nucl. Mater. **363–365**, 658 (2007).

[21] A. Hassanein, V. Morozov, V. Sizyuk, V. Tolkach, and B. J. Rice, "EUV sources for lithography," in *HEIGHTS-EUV Package for DPP Source Modeling*, edited by V. Bakshi (SPIE, Bellingham, WA, 2006), Chap. 9, p. 277.

[22] G. V. Miloshevsky, V. A. Sizyuk, M. B. Partenskii, A. Hassanein, and P. C. Jordan, J. Comput. Phys. **212**, 25 (2006).

[23] G. Tóth and D. Odstrčil, J. Comput. Phys. **128**, 82 (1996).

[24] A. Kirschner, V. Philipps, J. Winter, and U. Kögler, Nucl. Fusion **40**, 989 (2000).

[25] R. Samtaney, S. C. Jardin, P. Colell, and D. F. Martin, Comput. Phys. Commun. **164**, 220 (2004).

[26] M. T. Robinson, Radiat. Eff. Defects Solids **130-131**, 3 (1994).

[27] V. B. Berestetskii, E. M. Lifshitz, and L. P. Pitaevskii, *Quantum Electrodynamics*, 2nd ed. (Butterworth-Heinemann, 1982), Vol. 4.

[28] T. A. Mehlhorn, J. Appl. Phys. **52**, 6522 (1981).

[29] J. F. Ziegler, *The Stopping and Ranges of Ions in Matter: Handbook of Stopping Cross-Sections for Energetic Ions in All Elements* (Pergamon, 2013).

[30] A. Hassanein, V. Sizyuk, T. Sizyuk, and V. Morozov, Proc. SPIE **6517**, 65171X (2007).

[31] E. M. Henley and A. Garcia, *Subatomic Physics*, 3rd ed. (World Scientific Publishing Co. Pte. Ltd., 2007).

[32] I. Neumann, "Varions techniques in connection with random digits," NBS Appl. Math, Ser. **12**, 36 (1951).

[33] C. Pan, S. Wang, and J. Ou, Nucl. Fusion **54**, 103003 (2014).

[34] J. Shiraishi, N. Miyato, G. Matsunaga, M. Toma, M. Honda, T. Suzuki, M. Yoshida, N. Hayashi, and S. Ide, Nucl. Fusion **57**, 126051 (2017).

[35] J. Lin, W. Zhang, P. Liu, Z. Lin, C. Dong, J. Cao, and D. Li, Nucl. Fusion **58**, 016024 (2018).

[36] W. H. Barkas, R. W. Deutsch, F. C. Gilbert, and C. E. Violet, Phys. Rev. **86**(1), 59 (1952).

[37] D. B. Thomas and W. Luk, IET Comput. Digit. Tech. **1**, 312 (2007).

[38] V. Sizyuk and A. Hassanein, Nucl. Fusion **49**, 095003 (2009).

[39] F. Herman and S. Skillman, *Atomic Structure Calculations* (Prentice Hall, Englewood Cliffs, 1963).

[40] J. H. Hubbell, H. A. Gimm, and I. Overbo, J. Phys. Chem. Ref. Data **9**, 1023 (1980).

[41] V. Sizyuk, A. Hassanein, V. Morozov, V. Tolkach, T. Sizyuk, and B. Rice, Numer. Heat Tr., A-Appl. **49**, 215 (2006).

[42] V. Morozov, V. Tolkach, and A. Hassanein, "Calculation of tin atomic data and plasma properties," Argonne National Laboratory Report No. ANL-ET/02-23, Argonne, IL, 2002.

[43] V. Tolkach, V. Morozov, and A. Hassanein, "Development of comprehensive models for opacities and radiation transport for IFE systems," Argonne National Laboratory Report No. ANL-ET-04/24, Argonne, IL, 2004.

[44] D. Zaltzmann, *Atomic Physics in Hot Plasmas* (Oxford University Press, New York, 1998), Chap. 4.

[45] A. J. Webster, Nucl. Fusion **52**, 114023 (2012).

[46] O. V. Diyankov, I. V. Glazyrin, and S. V. Koshelev, Comput. Phys. Commun. **106**, 76 (1997).

[47] Y. Ueda, K. Schmid, M. Balden, J. W. Coenen, T. Loewenhoff, A. Ito, A. Hasegawa, C. Hardie, M. Porton, and M. Gilbert, Nucl. Fusion **57**, 092006 (2017).

[48] J. W. Coenen, V. Philipps, S. Brezinsek, G. Pintsuk, I. Uytdenhouwen, M. Wirtz, A. Kreter, K. Sugiyama, H. Kurishita, Y. Torikai, Y. Ueda, U. Samm, and the TEXTOR-Team, Nucl. Fusion **51**, 083008 (2011).

[49] Bebop cluster, Laboratory Computing Resource Center, Argonne National Laboratory, see http://www.lcrc.anl.gov/systems/resources/bebop/#facts.

[50] A. Hassanein, T. Sizyuk, and M. Ulrickson, Fusion Eng. Des. **83**, 1020 (2008).

[51] A. Hassanein and T. Sizyuk, Nucl. Fusion **48**, 115008 (2008).

[52] H. Reimerdes, G. P. Canal, B. P. Duval, B. Labit, T. Lunt, W. A. J. Vijvers, S. Coda, G. De Temmerman, T. W. Morgan, F. Nespoli, B. Tal, and the TCV Team, Plasma Phys. Controlled Fusion **55**, 124027 (2013).

[53] D. D. Ryutov and V. A. Soukhanovskii, Phys. Plasmas **22**, 110901 (2015).